Phase structure of completely asymptotically free SU(N_c) models with quarks and scalar quarks

F. F. Hansen,[1,*] T. Janowski,[1,†] K. Langæble,[1,‡] R. B. Mann,[2,§] F. Sannino,[1,3,4,‖] T. G. Steele,[5,¶] and Z. W. Wang[1,2,**]

[1]*CP^3-Origins, University of Southern Denmark, Campusvej 55 5230 Odense M, Denmark*
[2]*Department of Physics, University of Waterloo, Waterloo, Ontario N2L 3G1, Canada*
[3]*Theoretical Physics Department, CERN, 1211 Geneva, Switzerland*
[4]*Danish IAS, University of Southern Denmark, 5230 Odense, Denmark*
[5]*Department of Physics and Engineering Physics, University of Saskatchewan, Saskatoon, Saskatchewan S7N 5E2, Canada*

(Received 4 July 2017; published 21 March 2018)

We determine the phase diagram of completely asymptotically free SU(N_c) gauge theories featuring N_s complex scalars and N_f Dirac quarks transforming according to the fundamental representation of the gauge group. The analysis is performed at the maximum known order in perturbation theory. We unveil a very rich dynamics and associated phase structure. Intriguingly, we discover that the completely asymptotically free conditions guarantee that the infrared dynamics displays long-distance conformality, and in a regime when perturbation theory is applicable. We conclude our analysis by determining the quantum corrected potential of the model and summarizing the possible patterns of radiative symmetry breaking. These models are of potential phenomenological interest as either elementary or composite ultraviolet finite extensions of the standard model.

DOI: 10.1103/PhysRevD.97.065014

I. INTRODUCTION

Gauge theories featuring gauge, scalar, and fermion degrees of freedom constitute the back-bone of the standard model of particle interactions. It is therefore important to unveil their perturbative and nonperturbative dynamics.

Furthermore according to their ultraviolet properties these models can be classified into fundamental and effective low energy descriptions. Fundamental theories are, according to Wilson, the ones featuring in the UV noninteracting (free) [1–4] or interacting (safe) [5,6] fixed points. If multiple couplings are present, one can have complete asymptotic freedom (CAF) [1,7–14], or safety (CAS) [6,15,16], or mixed possibilities [12,16,17]. Exact nonperturbative results on the possible asymptotically (un)safe nature of supersymmetric gauge theories were investigated in [18] impacting the very existence of time-honored super grand unified theories [19]. The existence of controllable nonsupersymmetric models with interacting UV fixed points led to the recent discovery [20] that the addition of positive mass-squared terms leads to calculable radiative symmetry breaking in the IR, a phenomenon akin to the radiative symmetry breaking that occurs in the supersymmetric standard model [21]. We will not consider gravitational corrections which, however, are the subject of interesting related work [22–24].

Here we focus our attention on the dynamics of $SU(N_c)$ gauge theories with N_s complex scalars and N_f Dirac quarks transforming in the fundamental representation of the gauge group. Despite the in-depth study within the supersymmetric context mostly due to the remarkable work by Intriligator and Seiberg [25], very little is known about the nonsupersymmetric version with only one complex species of scalar quarks in addition to the ordinary quarks.

We therefore wish to partially close this gap by providing an in depth study of these models within a perturbative RG analysis along with the study of the associated quantum effective potential in the fully calculable regime. We discover a very rich physics associated to the various possible phases in which the models can be.

The choice to study these models stems from the past and recent interest in elementary [1,7–12,14] and composite extensions of the standard model featuring scalar quarks both in models of (super) bosonic technicolor [26–29] as

*ffhansen@cp3.sdu.dk
†janowski@cp3.sdu.dk
‡langaeble@cp3.sdu.dk
§rbmann@uwaterloo.ca
‖sannino@cp3.sdu.dk
¶tom.steele@usask.ca
**wang@cp3.sdu.dk

well as in models of composite Higgs dynamics [30–32] embodying explicit realizations [33,34] of the partial composite mechanism for standard model mass generation [35]. The underlying realizations[1] of these composite extensions are dubbed "*fundamental partial composite theories*" [33].

For the models at hand, we first investigate the CAF conditions. We then examine the infrared dynamics of the unveiled CAF models to the maximum known order in perturbation theory, allowing us to determine the perturbative phase diagram. Since models with scalars can undergo a radiative symmetry-breaking phenomenon because of the Coleman Weinberg (CW) mechanism [38], we carefully investigate this possibility here using the improved Gildener Weinberg (GW) approach [39,40]. We show that under certain conditions these models feature, besides CAF, also large distance conformality.

We now lay out the structure of the paper. In Sec. II, we introduce the models, their beta functions and spell out the conditions for CAF. We move to show the emergence of controllable interacting infrared fixed points to the maximum known order in perturbation theory. We discover that the phase diagram is rich and that the CAF conditions lead also to infrared conformality, at least in some coupling direction. Spontaneous radiative symmetry breaking is analyzed in Sec. III. Here we pay special attention to the possible patterns of symmetry breaking in the scalar sector. The analysis is performed in steps, with the zeroth order corresponding to a tree-level analysis and the quantum corrections studied at the one-loop order. The presence of multiple couplings leads to different limits in the parameter space of the model that can affect the radiative breaking scenarios. We conclude in Sec. IV and add a number of appendixes containing further technical details.

II. ULTRAVIOLET AND INFRARED PROPERTIES OF THE MODEL

In this paper, we consider an $SU(N_c)$ gauge theory involving N_s complex scalars S and N_f vector-like fermions Q in the fundamental representation (see Table I). The Lagrangian is

$$\mathcal{L} = -\frac{1}{2}\mathrm{Tr}F^{\mu\nu}F_{\mu\nu} + \mathrm{Tr}(\bar{Q}i\not{D}Q) + \mathrm{Tr}(D_\mu S^\dagger D^\mu S) - v(\mathrm{Tr}S^\dagger S)^2 - u\mathrm{Tr}(S^\dagger S)^2, \tag{2.1}$$

where $F_{\mu\nu} = F^I_{\mu\nu}t^I (I = 1\cdots, N_c^2 - 1)$ is the field strength tensor and t^I are the SU(N_c) generators in the fundamental representation satisfying $\mathrm{Tr}(t^I t^J) = (1/2)\delta^{IJ}$. We use A, B, C, D to denote color indices in the fundamental representation, I, J, K, L in the adjoint representation, and a, b, c, d to denote the flavor index in the fundamental representation of $U(N_s)$). In our notation, the fermion fields Q and the scalar fields S are rectangular matrices with dimensions $N_f \times N_c$ and $N_s \times N_c$ (i.e. S_{aA}), respectively.

TABLE I. Matter field content of the model including the quantum symmetry group. Fermion fields are presented in the left-handed spinor convention.

	Gauge symmetries	Global symmetries		
Fields	$SU(N_c)$	$SU(N_f)_L$	$SU(N_f)_R$	$U(N_s)$
Q	$\square$	$\square$	1	1
$\tilde{Q}$	$\overline{\square}$	1	$\overline{\square}$	1
S	$\square$	1	1	$\square$

Note that for specific color choices, with $N_c \leq 4$ and $N_s \leq 4$, additional renormalizable terms in the Lagrangian appear. Here for example for $N_c = N_s$ we can construct the operator $\det S$. Similarly, for $N_c = 4$ and $N_s = 2$ or $N_c = 2$ and $N_s = 4$ we have terms, which for the latter case can be written as $\varepsilon_{AB}\varepsilon_{CD}\varepsilon^{abcd}S^A_a S^B_b S^C_c S^D_d$. Furthermore for $N_c = 3$ a Yukawa term can be written involving one scalar and two quarks. Additional terms of these types would give additional contributions to the beta functions, which are not considered in this work.

A. UV behavior: Completely asymptotically free (CAF)

Since the model has three marginal couplings we now investigate its ultraviolet behavior and establish the conditions under which it can be completely asymptotically free. We are interested in characterizing the flow behavior around the Gaussian fixed point, and therefore one can use one-loop expressions for the beta functions.

Using the rescaled couplings, i.e. $\alpha = g^2/(4\pi)^2$, $\lambda_1 = v/(4\pi)^2$, $\lambda_2 = u/(4\pi)^2$, the one-loop beta functions (first calculated in [33], with general RG functions to two-loop order provided in [41]) are

$$\begin{aligned}
\beta_\alpha &= -\frac{1}{3}(22N_c - 4N_f - N_s)\alpha^2 \\
\beta_{\lambda_1} &= 4(N_cN_s + 4)\lambda_1^2 + 12\lambda_2^2 \\
&\quad + \lambda_1\left[8(N_c + N_s)\lambda_2 - \frac{6(N_c^2 - 1)}{N_c}\alpha\right] + \frac{3(N_c^2 + 2)}{4N_c^2}\alpha^2 \\
\beta_{\lambda_2} &= 4(N_c + N_s)\lambda_2^2 + \lambda_2\left[24\lambda_1 - \frac{6(N_c^2 - 1)}{N_c}\alpha\right] \\
&\quad + \frac{3(N_c^2 - 4)}{4N_c}\alpha^2.
\end{aligned} \tag{2.2}$$

We note that, to this order, the gauge beta function only depends on the gauge coupling, and it is of the form $\beta_\alpha = -B\alpha^2$. Requiring asymptotic freedom (AF), is equivalent to restricting the coefficient B to be positive. The

[1] A list of underlying fundamental theories for near conformal dynamics and composite Higgs models, before considering fermion mass generation, can be found in [36,37].

critical number of fermion flavors, N_f^*, for which asymptotic freedom is lost in the gauge coupling, $B = 0$, is $N_f^* = (22N_c - N_s)/4$. The gauge coupling will be AF for models with non-negative integer values $N_f < N_f^*$. We thus have an upper bound on N_s, i.e. $N_s \leq 22N_c$.

The two beta functions for the quartic couplings depend on all three couplings but only on N_c and N_s. At sufficiently high energies, the scalar potential of a CAF model is well approximated by the tree-level terms

$$V = \lambda_1(\mathrm{Tr}S^\dagger S)^2 + \lambda_2 \mathrm{Tr}(S^\dagger S)^2 \tag{2.3}$$

This potential is positive definite for values of the couplings satisfying $\lambda_1 + r\lambda_2 > 0$ for all $r = \mathrm{Tr}(S^\dagger S)^2/(\mathrm{Tr}S^\dagger S)^2$, which ranges from $1/\min(N_c, N_s)$ and 1. Note that this allows one of the two couplings to be negative, but not both simultaneously.

For CAF to exist we first need to find solutions to the following fixed flow relation,

$$(\beta_\alpha, \beta_{\lambda_1}, \beta_{\lambda_2}) = c(\alpha, \lambda_1, \lambda_2), \tag{2.4}$$

for a nonzero scale-dependent coefficient c. In Appendix A, we discuss how Eq. (2.4) is related to other, equivalent CAF requirements. When the gauge coupling is zero, $\alpha = 0$, the quartic couplings are only asymptotically free along lines that correspond to unstable scalar potentials, Eq. (2.3).

We will now outline the criteria under which solutions exist and count the number of solutions. The fixed flow solution for $\alpha > 0$ will necessarily satisfy $c = -B\alpha$, which can be substituted into the remaining equations. Since β_{λ_2} depends linearly on λ_1, we can easily solve for $\lambda_1(\lambda_2, \alpha)$ and substitute this into the equation for β_{λ_1}. The result is a quartic equation in λ_2. The coefficients of this equation depend on N_c, N_s, B. Introducing the quantity $N_x = N_f^* - N_f$, we can express $B = 4N_x/3$. The number of fixed flow solutions corresponds to the number of real roots of the quartic polynomial, which can be calculated using the discriminant method. The full expression for the quartic polynomial and the expressions for classifying the nature of the roots can be found in Appendix B. For a fixed value of N_x, we find a region with two distinct real solutions (region I) and a smaller region with four distinct real solutions (region II). The upper border of region II is shared with region I.

In Fig. 1, we show how the borders of these regions change when varying the number of fermion flavors ($N_x \in \{0, 1, 2, 3, 4\}$). It should be noted, that for small values of N_x, the effect of increasing N_x is to move the upper border of region I downward, while the borders of region II largely remains unchanged. Furthermore, we note that in the limit $N_x = 0$ ($N_f = N_f^*$), Eq. (2.4) no longer describes fixed flows, since the one-loop beta function for the gauge coupling is vanishing and higher-order terms will dictate the running. Nonetheless, solving the quartic function with $N_x = 0$ corresponds to finding fixed points in the subsystem β_{λ_1}, β_{λ_2} and is closely related to finding infrared fixed points for the full model (see more details in later section). The region with two distinct sets of solutions for $N_x = 0$ is marked with light gray in Fig. 1, while the region with four distinct sets of solutions is marked with gray. From Fig. 1, we see that for fixed values of $N_s \geq 2$ and $N_x > 0$, there exists a lower bound of N_c above which the models have two fixed flow solutions For even higher values of N_c, two additional fixed flow solutions appear. Increasing either N_x (i.e. lowering N_f) or N_s will push the lower bound on N_c towards higher values, whereas the transition from two to four fixed flow solutions is only mildly dependent on N_x. In Table II, the values of N_c, N_s, N_f for models with CAF are tabulated.

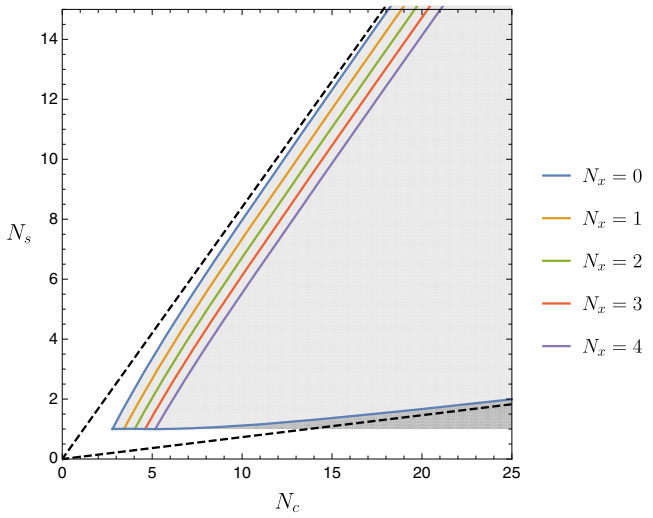

FIG. 1. Regions in N_c, N_s for constant N_x for which the model is CAF. The solid lines show the borders of the region with two fixed flow solutions (region I) for $N_x \in \{0, 1, 2, 3, 4\}$ The blue boundary $N_x = 0$ represents a limit and does not satisfy CAF. The light gray (dark gray) region marks the region where two (four) real distinct sets of solutions exist for the limiting case $N_x = 0$. The dashed black lines are the asymptotic behavior of the borders of the two fixed flow solution region.

Existence of fixed flows only implies that specific directions flow out of the Gaussian fixed point. However, to complete the picture, we need information about the behavior of the RG trajectories in the neighborhood of the fixed flow lines. To investigate this, we parametrize the couplings $(\alpha, \lambda_1, \lambda_2)$ using spherical coordinates,

$$\alpha = r\sin\theta\cos\phi, \quad \lambda_1 = r\sin\theta\sin\phi, \quad \lambda_2 = r\cos\theta, \tag{2.5}$$

and obtain expressions for the RG beta functions of (r, θ, ϕ), i.e. $(\beta_r, \beta_\theta, \beta_\phi)$.

TABLE II. Windows in N_f for $N_s = \{2, 9\}$, $N_c = \{5, 12\}$ for which the model is CAF, i.e. allow for fixed flow solutions to Eq. (2.4). There exist two fixed flow solutions for every value of N_f in each window. There are no solutions for $N_c = \{3, 4\}$ and $N_s > 1$.

	$N_c = 5$	$N_c = 6$	$N_c = 7$	$N_c = 8$	$N_c = 9$	$N_c = 10$	$N_c = 11$	$N_c = 12$
$N_s = 2$	25–26	29–32	33-37	37–43	41–48	44–54	48–59	52–65
$N_s = 3$		31–32	35–37	38–43	42–48	46–54	50–59	54–65
$N_s = 4$			36–37	40–42	44–48	48–53	52–59	55–64
$N_s = 5$			37	41–42	45–48	49–53	53–59	57–64
$N_s = 6$					47	51–53	55–58	59–64
$N_s = 7$						52–53	56–58	60–64
$N_s = 8$							58	62–63
$N_s = 9$								63

At one loop, the beta functions, β_θ, β_ϕ, depend only multiplicatively on the radial coordinate, i.e. $\beta_{\theta,\phi} = r f_{\theta,\phi}(\theta, \phi)$, and the direction (θ, ϕ), therefore, does not depend on r. Factoring out the radial coordinate r, we can examine the UV behavior in a reduced space of only two parameters. This is shown in Fig. 2 for a model in region I (top panels) and a model in region II (bottom panels), with the arrows pointing from UV to IR.

In order for a trajectory to be connected to the Gaussian UV fixed point, the radial coordinate has to go to zero in the UV. Within the one-loop approximation, the change in r is of the form $\beta_r = r^2 f_r(\theta, \phi)$. The radial

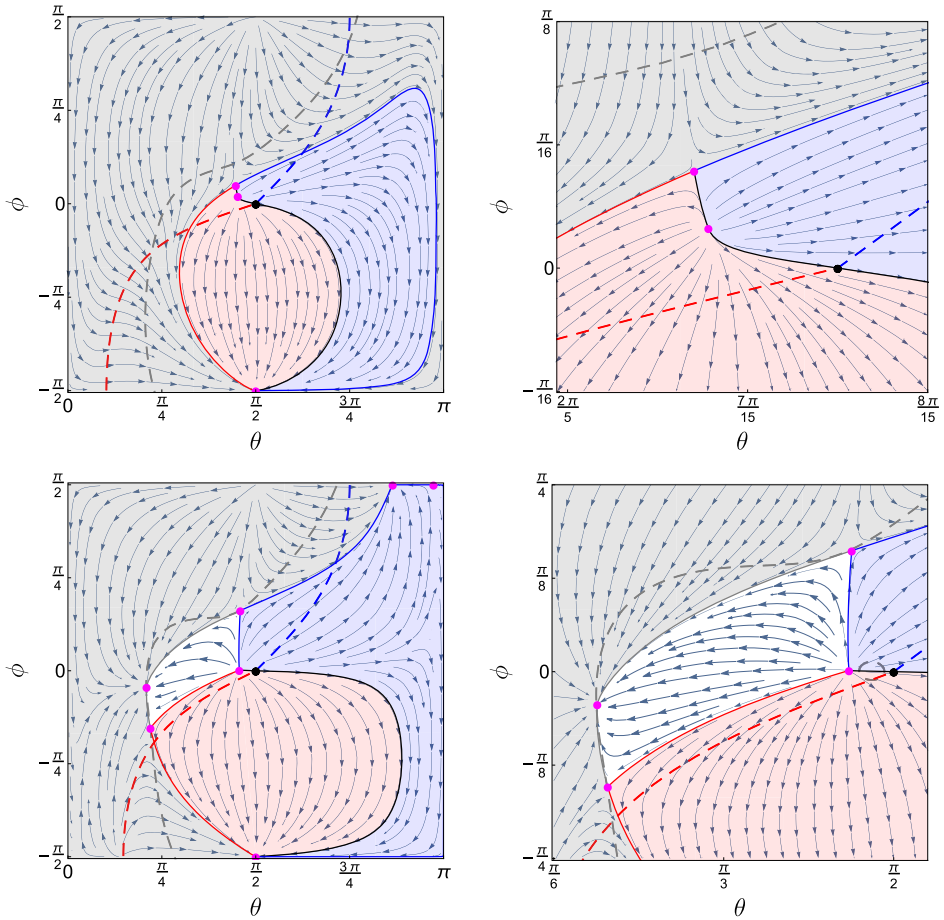

FIG. 2. UV behavior around the fixed flow solutions in spherical coordinates (θ, ϕ). Upper left: Full phase space in case of two fixed flow solutions. Upper right: Close-up at the region close to the two fixed points. Lower left: Full phase space in case of four fixed flow solutions. Lower right: Close-up at the region close to the four fixed points. UV divergent flows are in grey regions. Flows between fixed flows that do not cross the tree-level instability lines are in white regions; those that do cross are in red or blue regions depending on which quartic coupling is negative.

coordinate is, thus, only decreasing in regions of (θ, ϕ) where $f_r(\theta, \phi) < 0$. In Fig. 2, the transition $(f_r(\theta, \phi) = 0)$ is shown as dashed grey lines. The regions with flows that cross this line and are, thus, not connected to the Gaussian UV fixed point, are colored grey. Similarly, we mark the regions with red and blue, where the flows cross the conditions for a bounded tree-level potential (dashed red and blue lines) depending on which quartic coupling is negative.

We show the UV behavior for the full phase space in the case of two solutions in the upper left panel of Fig. 2 and a close-up of the region around the two fixed flow points in the upper right panel. We note that one point is completely repulsive, while the other has one repulsive direction and one attractive direction (mixed). For the mixed case, the repulsive directions (the red and blue solid lines) separate the flows with UV asymptotic freedom (the red and blue shaded regions) from the ones that are UV divergent, i.e. the grey region. The attractive direction (the black line between two fixed flow points) separates the two tree-level symmetry-breaking regions. In the lower two panels of Fig. 2, we show the case of four fixed flow solutions. In this case, the two additional fixed points for the fixed flow open up a two-dimensional region where the flows are between fixed points without crossing the tree-level symmetry-breaking lines. This region is marked with white. One of the two additional fixed points for the fixed flows is fully attractive, while the other is with mixed properties. For the fully attractive one, only this exact relation of the three couplings is connected to the UV. This case therefore offers full predictability in the IR. This will be further discussed in Sec. II C.

In the results discussed above, we factor out the r-dependence of the couplings, which is valid within the one-loop approximation of the beta functions. Therefore Fig. 2 is only adequate for describing the behavior close to the Gaussian UV fixed point. Starting from a point where $r \ll 1$, such that the beta functions are well approximated by the one-loop expressions, we trust the flows in the backward direction (towards higher energies) outside the grey regions, since r is decreasing. On the contrary, we cannot follow the flows too far forwards, since the approximation is getting worse (r increasing). However, we note that the change in r is generally suppressed by a factor of r compared to the change in θ and ϕ, except at points close to the fixed flow directions, where $f_{\theta,\phi}(\theta, \phi) \sim 0$. This means that the relations among the three couplings can change substantially while the one-loop approximation is still valid. Seen from the UV perspective of the Gaussian fixed point (one-loop approximation), we expect the four-solution case to offer more possibilities to flow from the UV Gaussian fixed point to a possible IR fixed point because of the fully attractive fixed flow solution, which provides a region that seemingly does not cross the symmetry-breaking lines.

Here we summarize our conclusions from restricting the model to be CAF:

(i) In Fig. 1, we show the region in N_s and N_c within which there exists a window in N_f (with upper endpoint given by N_f^*), for which the models are CAF. We note that $N_c > N_s$ in the whole region.
(ii) The size of the window depends on the position in the grey region of Fig. 1. Close to the upper border (i.e. $N_x = 0$ line) of the light grey region, the size of the window is vanishing. This behavior is evident from Table II, where we show the range of the window in N_f for the lowest combinations of N_s and N_c.
(iii) In Fig. 2, we illustrate the UV behavior in the vicinity of the Gaussian fixed point. In the two fixed flow solution case, there is one fully UV attractive direction and one with mixed properties. In the four fixed flow solution case, one of the two additional directions is fully UV repulsive while the other is mixed.

B. Long distance conformality

In Fig. 1, we see that the whole region in N_s and N_c corresponding to CAF models is contained in the region with $N_x = 0$. In Appendix B, we show that the existence of solutions to Eq. (2.4) for $N_x = 0$, guaranties the existence of fixed points to the one-loop $(\beta_{\lambda_1}, \beta_{\lambda_2})$-subsystem, where α is treated as any nonzero, positive scale-dependent value.

In other words, if the gauge coupling has a fixed point ($\beta_\alpha = 0$), then we already know that there exist values λ_1, λ_2 satisfying $\beta_{\lambda_1} = 0$, $\beta_{\lambda_2} = 0$ at one loop in the quartic subsystem. Following the ordering from the Weyl-consistency conditions [42–44], we should treat the system at three loops in the gauge beta function together with the one-loop quartic beta functions. To keep the analysis in the main section light, we study here the two-loop gauge beta function together with the one-loop quartic beta functions, while the full result is presented in the Appendix D. At this order, the running of the gauge coupling still decouples from the quartic couplings. We derive the gauge fixed point, and compute the accompanying fixed points values of the quartic couplings. We find that in most cases all three couplings at the fixed points are perturbatively small, and we therefore do not expect the three-loop contributions to the running of the gauge couplings to quantitatively change the preliminary findings of the this section. In fact, we find that each higher-loop order contribution will be suppressed by a factor of N_x/N_c. This, on the other hand, requires us to restrict our IR analysis to models close to losing AF, such that $N_x \ll N_c$, to achieve perturbative control of the loop expansion. In the generalized Veneziano limit, where N_c, N_s, $N_f \to \infty$ in such a way that all ratios are kept constant, the loop suppression can be arbitrarily small, whereas for

finite values of N_f, N_s and N_c the smallest value for N_x is $N_x = 1/4$. Further details are found in Appendix D.

If we write the two-loop gauge beta function as $\beta_\alpha = -B\alpha^2 + C\alpha^3$, then the nontrivial fixed point occurs for $\alpha^* = B/C$. For $B > 0$ and $C > 0$, this is an IR fixed point. The two-loop coefficient for the gauge beta function takes the form

$$C = \frac{8}{3}N_c N_s - \frac{68N_c^2}{3} - \frac{2N_f}{N_c} + \frac{26N_c N_f}{3} - \frac{2N_s}{N_c} \tag{2.6}$$

The critical number of fermion flavors for this coefficient to be positive is

$$\bar{N}_f = \frac{34N_c^3 - 4N_c^2 N_s + 3N_s}{13N_c^2 - 3} \tag{2.7}$$

and since in our case, where $N_c > 2$, we always have that $N_f^* > \bar{N}_f$, the functions $\bar{N}_f$ and N_f^* define the window of existence for the infrared fixed point in the gauge coupling. From requiring the model to be CAF, we already know from the UV analysis, that if the gauge beta function has a nontrivial fixed point, then so does the quartic coupling subsystem. Therefore, the window for the existence of IR fixed points is the grey region in Fig. 1 for N_f within $N_f \in [\bar{N}_f, N_f^*]$. The result is summarized in Table III, where the fixed points are determined numerically, and nonperturbative fixed points ($\alpha, \lambda_i > 1$) have been discarded. Comparing Table II with Table III, we conclude that the CAF condition is stronger than the condition for the existence of IR fixed points, meaning that any CAF model of this kind always possesses IR fixed points to this order in perturbation theory.

In order for the results not to be significantly altered by higher-order contributions, we need to show that these higher-loop contributions are suppressed. This is shown in Appendix D. Here it is sufficient to say that a Banks-Zaks-like analysis [45,46] is possible.

In the following, we will characterize the IR fixed points. To find eigendirections of the IR fixed points, we need to study the following matrix:

$$M = \left.\begin{pmatrix} \frac{\partial\beta_\alpha}{\partial\alpha} & \frac{\partial\beta_\alpha}{\partial\lambda_1} & \frac{\partial\beta_\alpha}{\partial\lambda_2} \\ \frac{\partial\beta_{\lambda_1}}{\partial\alpha} & \frac{\partial\beta_{\lambda_1}}{\partial\lambda_1} & \frac{\partial\beta_{\lambda_1}}{\partial\lambda_2} \\ \frac{\partial\beta_{\lambda_2}}{\partial\alpha} & \frac{\partial\beta_{\lambda_2}}{\partial\lambda_1} & \frac{\partial\beta_{\lambda_2}}{\partial\lambda_2} \end{pmatrix}\right|_{\alpha=\alpha^*,\lambda_1=\lambda_1^*,\lambda_2=\lambda_2^*}, \tag{2.8}$$

where $(\alpha^*, \lambda_1^*, \lambda_2^*)$ corresponds to the coupling solutions at the IR fixed points. In the convention that the RG flow runs from UV to IR, the positive (negative) eigenvalues represent IR attractive (repulsive) directions. In the region, where we have perturbative control of our IR fixed points, they inherit their characteristics from the corresponding fixed flow solutions. The third eigendirection, which is not part of the fixed flow picture (Fig. 2), is dominated by the gauge coupling, and is always IR attractive. Within the region with two IR fixed points, we have one, which has two repulsive eigendirections, while the other fixed point has one repulsive and one attractive eigendirection. Combined with the third eigendirection, we can conclude that the one with two repulsive directions is only connected to the UV along a single trajectory, while the other one is connected through a one parameter family of trajectories. These trajectories all originate from the fully repulsive fixed flow direction. There is also a trajectory connecting the two IR fixed points. In Fig. 3, we show the flow behavior around the IR fixed points on the plane of constant $\alpha = \alpha^*$ in spherical coordinates. This allows us to see the similarities with the UV picture (Fig. 2). In the case with four IR fixed points, we have additionally one fixed point with mixed properties and one which is fully IR attractive. Unlike from the previous case, the fully IR attractive fixed point has a three dimensional basin of attraction, implying IR conformal stability in all directions. In Fig. 3, this is illustrated by a two dimensional region, since α is kept fixed. In Table IV, we provide a summary of the IR fixed points.

We learn that CAF models with spin zero and spin half quarks also feature IR interacting fixed points. In Appendix C, we explore the connection in detail. In short, we can show that for fixed flows to exist with both λ_1 and λ_2 positive, there must be fixed points in the quartic subsystem of beta functions. These fixed points correspond fixed

TABLE III. Window in N_f that allow for IR fixed points with perturbative couplings, i.e. $\alpha, \lambda_i < 1$ for $N_s = \{2, 9\}$, $N_c = \{4, 12\}$. There are no solutions for $N_c = 3$ for $N_s > 1$.

	$N_c = 4$	$N_c = 5$	$N_c = 6$	$N_c = 7$	$N_c = 8$	$N_c = 9$	$N_c = 10$	$N_c = 11$	$N_c = 12$
$N_s = 2$	11–21	14–26	16–32	19–37	21–43	24–48	27–54	29–59	32–65
$N_s = 3$		13–26	16–32	18–37	21–43	24–48	26–54	29–59	31–65
$N_s = 4$			16–31	18–37	21–42	23–48	26–53	29–59	31–64
$N_s = 5$				18–37	20–42	23–48	26–53	28–59	31–64
$N_s = 6$					20–42	23–47	25–53	28–58	31–64
$N_s = 7$						22–47	25–53	28–58	30–64
$N_s = 8$								27–58	30–63
$N_s = 9$									30-63

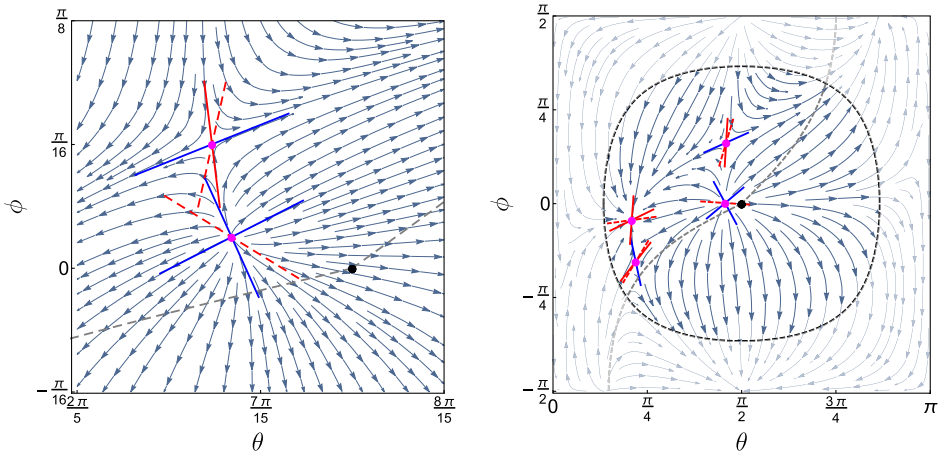

FIG. 3. IR flow behavior around the IR fixed points in spherical coordinates (θ, ϕ) with α kept fixed at the IR fixed point, $\alpha_* = B/C$. Left: Close-up of the case with two IR fixed points. Right: Full phase space in the case of four IR fixed points. Each fixed point (magenta dot), has its eigendirections superimposed. Color coding: Red is IR attractive, Blue IR repulsive. The red dashed lines are the projections of the third eigen-directions (IR attractive) of the fixed point in (r, θ, ϕ) onto the (θ, ϕ)-subspace. The shaded white region marks the region in (θ, ϕ), where the quartic couplings become comparable to the gauge coupling at the fixed point, $\lambda_1^2 + \lambda_2^2 = 5\alpha_*^2$, and higher-order corrections are expected.

points for the full system since the gauge coupling has an IR fixed point as well ($C > 0$ in the region with fixed points in the subsystem). The case where both λ_1 and λ_2 are negative can be discarded by demanding a bounded scalar potential in the UV. The cases with one of the quartic coupling negative, could be realized without the existence of fixed points in the subsystem. However, for the particular N_c and N_s dependence of the coefficients for this model, this does not occur.

C. Phase diagram

From the previous section, we know there exist two kinds of phase structures; one with two IR fixed points and another with four IR fixed points. On one hand, the four IR fixed points case requires quite large number of colors N_c and flavors N_f even for small values of N_s. On the other hand, this scenario provides a fully IR predictive case. In other words, this group of models possesses a fully UV repulsive fixed flow, for which all relations among couplings are fixed, and we can thus fully determine the IR fate of the model at the highest known order in perturbation theory. We will in the following do this for the minimal choice of colors, i.e. $N_c = 26$, which in order to satisfy the CAF conditions requires $N_s = 2$ and $N_f = 138$. Afterwards, we will focus our attention on the general phases of the two types of phase structures. Note that, for simplicity, we assume all the particles to be massless. In general, the RG functions will be modified after symmetry breaking and a more sophisticated treatment will be required (e.g. threshold contributions need to be considered). In this sense, we only consider what happens until spontaneous symmetry breaking occur. A detailed study of the IR phases after symmetry breaking is beyond the scope of this work.

In Fig. 4, for our particular choice of N_c, N_s and N_f, we show the running of the couplings from the UV (with coupling ratios fixed by the fully repulsive fixed flow) towards the IR. We show the result from using both the

TABLE IV. Summary of IR fixed points and the number of their relevant and irrelevant eigenvalues.

Fixed point	Eigenvalue		
FP_1	+	−	−
FP_2	+	−	+
FP_3	+	+	+
FP_4	+	+	−

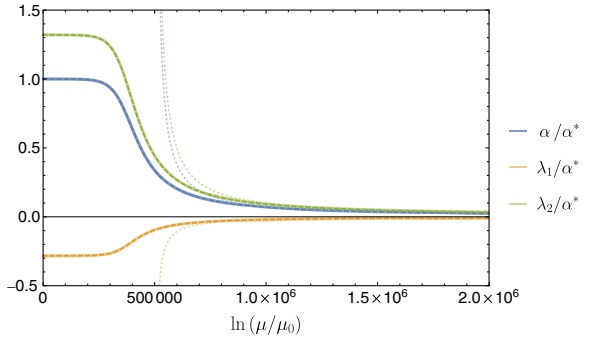

FIG. 4. Renormalization group running of all couplings from the fully IR attractive fixed point to the fully UV repulsive fixed flow. All couplings are normalized in units of α^*. We use the one-loop beta functions for the quartic couplings together with the one-loop (dotted), two-loop (dashed), and three-loop (solid) gauge beta function.

one-, two- and three-loop gauge beta function together with the one-loop beta function for the quartic couplings. It is evident, that both in the two-loop and three-loop gauge case, the IR fate of the model is long distance conformality.

Similarly, we can solve the differential equations for each direction out of the Gaussian UV fixed point, and determine the IR fate anticipating and using the symmetry-breaking conditions derived in Sec. III. In this way, we distinguish between three IR phases connected to the Gaussian UV fixed point. Long distance conformality (white) along with two kinds of spontaneous symmetry breaking (blue and red). Gray regions are not connected to the Gaussian UV fixed point.

In the left panel of Fig. 5, we show the result of this analysis for a representative model with the two IR fixed point phase structure. We see that practically all directions connected to the UV, lead to spontaneous symmetry breaking. On the separatrices of the two symmetry-breaking regions, we find fine-tuned solutions reaching the IR fixed points, and solutions crossing the intersection of the two symmetry-breaking lines.

In the right panel of Fig. 5, the phase diagram for the other phase structure with four IR fixed points is shown. Here we have all three IR phases present.

We notice that the phase diagrams are basically identical to the UV picture in Fig. 2. From this we conclude, that the lowest-order approximations to the symmetry-breaking conditions together with the one-loop beta functions are good indicators for the IR fate of CAF models. This is tightly connected to the relation between fixed flows in the UV and fixed points in the IR together with the fact that β_r is r-suppressed (in the UV) compared to β_θ and β_ϕ. However, for directions close to the fixed flows or the separatrices (where $\beta_r \sim \beta_{\theta,\phi}$) we need higher-order terms to correctly describe the RG evolution. Even so, for $r \ll 1$ the affected regions are not directly visible, except for the phase of long distance conformality in between the four fixed flows.

For values of the gauge coupling larger than the one at the IR fixed points, other phases exists. However, these are not UV free and are therefore outside the focus of this work.

In Fig. 6, we show the RG flow of the couplings projected onto the (α, λ_i)-planes and (λ_1, λ_2)-plane with the third coupling fixed. In each panel, we show the lines where spontaneous symmetry breaking occurs using the one-loop result from Sec. III B. In the upper left panel, it is clear that the flows above the fixed flow line are not originating from the UV Gaussian fixed point (blue dot), whereas the flows below (unless in the broken phase, marked with gray) all emanate from the fixed point along the other fixed flow line. The same features are seen in the upper right panel. In the lower left panel, we see that only flows in the broken phase originate from the Gaussian UV fixed point, when the gauge coupling is kept fixed, $\alpha = 0$. The lower right panel, shows the two IR fixed points on the plane $\alpha = \alpha^*$. We see that the symmetry-breaking lines both with $\alpha = 0$ and $\alpha = \alpha^*$ seem to be identical. This illustrates that for couplings less than or comparable to α^*, the tree-level result is still a good approximation. From these diagrams it is clear that the fixed points are all in the unbroken phase.

We have so far uncovered the conditions for the models to be completely asymptotically free and shown numerically that these conditions are stronger than the conditions for the existence of IR fixed points. Furthermore, we have described the phase structure of the models anticipating

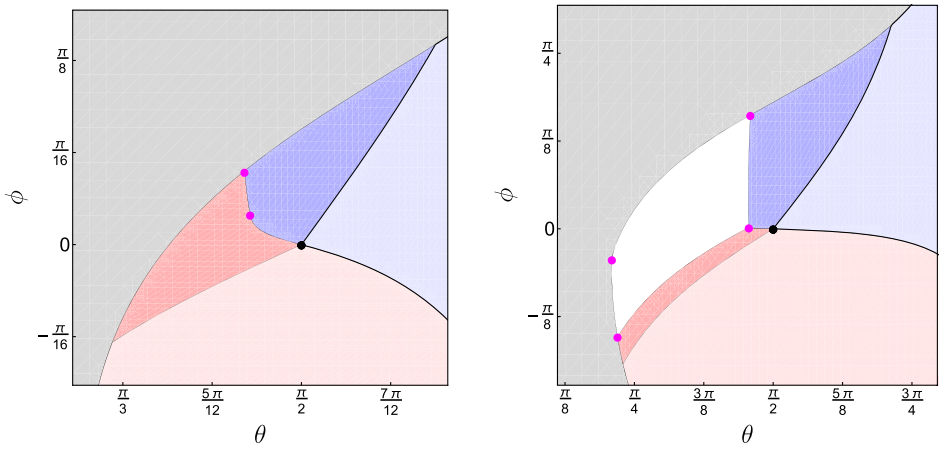

FIG. 5. Phase diagram for the case of two (four) fixed flows are shown in the left (right) panel in spherical coordinates θ and ϕ. The initial radial coordinate, r, is chosen close to the Gaussian fixed point, i.e. $r \ll 1$. The phases are then determined by analyzing the numerical solutions to the beta functions at three-loop order in the gauge coupling, together with the one-loop for the quartic couplings. The diagrams illustrate three IR phases connected to the Gaussian UV fixed point. Long distance conformality (white), two different spontaneous symmetry-breaking patterns (blue and red). Directions with trajectories not originating from the Gaussian UV fixed point are colored gray. The light red and light blue regions correspond to initial conditions with unbounded tree-level scalar potentials.

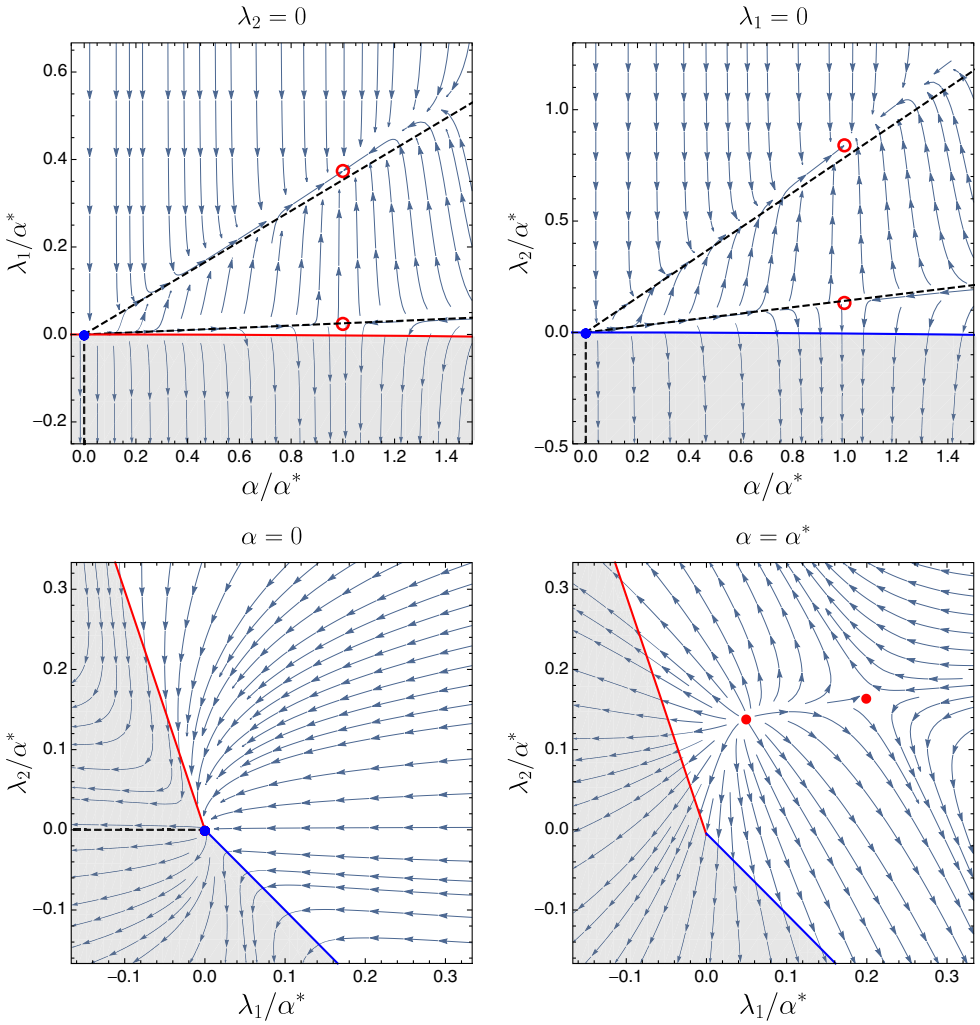

FIG. 6. Projected RG flow of the couplings onto the (α, λ_i)-planes (upper left and right) and (λ_1, λ_2)-plane with the third coupling fixed to $\alpha = 0$ (lower left) and $\alpha = \alpha^*$ (lower right). In each panel, we show the lines where spontaneous symmetry breaking occurs (red and blue) including one-loop effects. The gray regions here are the broken phases. Solid dots are fixed points in the full system, while circles mark fixed points in the reduced systems with one coupling kept fixed. Dashed lines mark the fixed flow lines for the reduced systems.

three infrared phases (two types of radiative symmetry breaking and a phase of long distance conformality) using conditions which will be derived in the following section.

III. SYMMETRY BREAKING

In order to understand the infrared phases of the models, we now address the question of radiative stability of the scalar potential. In this section, we will derive the tree-level stability conditions (flat directions) for the relevant vacuum configurations and derive their corresponding symmetry-breaking patterns. Afterwards, we will address the same problem beyond the tree-level analysis, referring the reader to the Appendix for the computational details.

A. Tree-level analysis

The tree-level analysis is the limiting case when the gauge contributions are turned off (i.e. $\alpha = 0$) and higher-order terms proportional to $\lambda^n (n > 1)$ are ignored. Thus, the boundary of the broken phase is a line in the $\lambda_1 - \lambda_2$ coupling space rather than a two-dimensional surface in the $\lambda_1 - \lambda_2 - \alpha$ space.

The tree-level potential has the following form:

$$V = m^2 \mathrm{Tr} S^\dagger S + \lambda_1 (\mathrm{Tr} S^\dagger S)^2 + \lambda_2 \mathrm{Tr}(S^\dagger S)^2, \quad (3.1)$$

where the $N_c \times N_s$ scalar field matrix S is invariant under $SU(N_c) \times U(N_s)$ rotations. For the scalar potential to be bounded from below, at sufficiently high-energy scales, the quartic couplings have to satisfy $\lambda_1 + r\lambda_2 > 0$ for all $r = \mathrm{Tr}(S^\dagger S)^2/(\mathrm{Tr} S^\dagger S)^2$, which ranges from $1/N_s$ and 1. To illustrate the symmetry-breaking pattern, it will be convenient to replace the traces with sums over the eigenvalues and subsequently find the minimum of the potential in the eigenvalue space. To that end, it will be useful to write the matrix S in the form

$$S(x) = U_c^\dagger(x) D(x) U_s(x), \tag{3.2}$$

where U_c and U_s are unitary matrices and D is a matrix which is diagonal in a $N_s \times N_s$ block (with real entries) and zero everywhere else, assuming that $N_c > N_s$ (which is true for the CAF conditions to be satisfied). Although this is a well-known result, we summarize the proof in Appendix E. We emphasize that this is not a local flavor and color transformation, but simply rewriting the matrices S in terms of different degrees of freedom. In the symmetry-breaking section, we are just interested in finding the vacuum configurations which are spacetime independent. Once the minimum is found, the matrix D can be rotated back to give the field value corresponding to the minimum in the original basis. As a result, this procedure does not give rise to additional terms from the kinetic part of the Lagrangian. Thus, the potential can be rewritten as

$$V = m^2 \mathrm{Tr} D^\dagger D + \lambda_1 (\mathrm{Tr} D^\dagger D)^2 + \lambda_2 \mathrm{Tr}(D^\dagger D)^2, \tag{3.3}$$

i.e. all the dependence on the unitary matrices U_c and U_s vanishes. The one-loop effective potential will likewise depend only on the components of D and so only the components of D can obtain nonzero vacuum expectation values.

The relevant degrees of freedom relevant in understanding the behavior of the effective potential are the diagonal part diag $(\rho_1, \rho_2, \ldots, \rho_{N_s})$ of D. The tree-level potential can, thus, be simplified into the following form,

$$V = m^2 \sum_{i=1}^{N_s} \rho_i^2 + \lambda_1 \left(\sum_{i=1}^{N_s} \rho_i^2 \right)^2 + \lambda_2 \sum_{i=1}^{N_s} \rho_i^4, \tag{3.4}$$

where m^2 could be positive, zero or negative. For a positive mass term, i.e. $m^2 > 0$, the potential has minimum at $\rho_i = 0$, and this excludes symmetry breaking, while for $m^2 < 0$, we will have spontaneous symmetry breaking as long as the potential is bounded. One can further show that the nontrivial vacuum configurations for the $m^2 < 0$ case at tree level are the same as in the massless cases at tree level (a detailed proof is in [47]).

Restricting to the $m^2 = 0$ case,[2] we will now follow Ref. [40] to determine the rays along which the potential vanishes. Without loss of generality we constrain the ρ_i's on an N_s-dimensional hypersphere, i.e. $\sum_{i=1}^{N_s} \rho_i^2 = l$. The constraint is imposed on the potential through a Lagrange multiplier L, leading to

$$V = \lambda_1 l^2 + \lambda_2 \sum_{i=1}^{N_s} \rho_i^4 + L \left(\sum_{i=1}^{N_s} \rho_i^2 - l \right). \tag{3.5}$$

The condition to minimize the potential is then given by

$$\frac{\partial V}{\partial \rho_j} = 4\lambda_2 \rho_j^3 + 2L\rho_j = 0, \tag{3.6}$$

providing the solutions

$$\rho_j^2 = -\frac{L}{2\lambda_2} \quad \text{or} \quad \rho_j^2 = 0. \tag{3.7}$$

It is clear that at the extrema of V on the sphere, all nonzero elements of ρ_i^2 will be equal. Suppose there are k nonzero elements with value ρ, then we find that $\rho^2 = \frac{l}{k}$, and we obtain

$$V|_{\text{ext}} = l^2 \left(\lambda_1 + \frac{\lambda_2}{k} \right). \tag{3.8}$$

When $\lambda_2 > 0$, the potential attains a minimal value at the extremum with k as large as possible, leading to $k = N_s$

$$V|_{\min} = l^2 \left(\lambda_1 + \frac{\lambda_2}{N_s} \right), \quad \text{for } \lambda_2 > 0, \tag{3.9}$$

whereas if $\lambda_2 < 0$, the potential will be minimal for $k = 1$, i.e.,

$$V|_{\min} = l^2(\lambda_1 + \lambda_2), \quad \text{for } \lambda_2 < 0. \tag{3.10}$$

In order for the direction to be flat, we require the $V|_{\min} = V(\rho_i = 0) = 0$ to obtain a ray on which loop effects can induce spontaneous symmetry breaking. These rays exist under two conditions:

$$\text{For } \lambda_2 > 0\text{: } N_s\lambda_1 + \lambda_2 = 0 \tag{3.11}$$

$$\text{For } \lambda_2 < 0\text{: } \lambda_1 + \lambda_2 = 0. \tag{3.12}$$

These lines are summarized in Fig. 7. In the figure, we overlap two sets of coordinates (λ_1, λ_2) and $(\lambda_{1s}, \lambda_{2s})$, with $\lambda_{is} = \lambda_i/\alpha$, for which the lines coincide. Requiring the potential to be bounded from below, implies the RG flow in the UV ($t \to \infty$) to be in region I. However for a completely asymptotically free model, $\lambda_i = 0$. To plot these models in the diagram, it is useful to use the alternative parameters λ_{is}, for which the UV fixed point is not at the origin. This condition was used in Sec. II A to correctly find the CAF models. For spontaneous symmetry breaking to occur, the RG flow (from UV to IR) must run from region I to region II regardless of the chosen set of coordinates.

[2]The massless case corresponds to classically conformal models which possess many interesting features such as providing naturally light Higgs in asymptotically safe or free scenarios [17] (see also earlier works [48–50]).

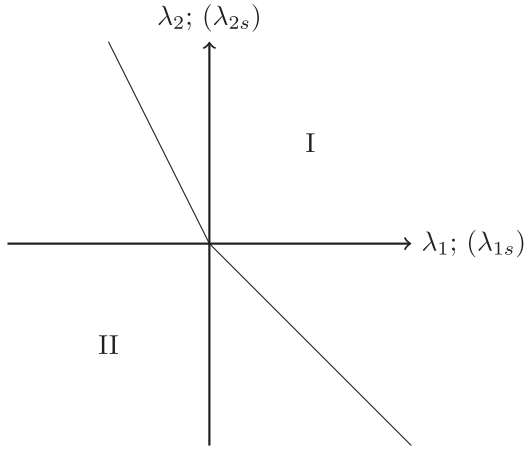

FIG. 7. Boundary lines in the parameter space $\lambda_1 - \lambda_2$ $(\lambda_{1s} - \lambda_{2s})$, with $\lambda_{is} = \lambda_i/\alpha$, across which symmetry breaking can occur. In region I, the tree-level potential is bounded from below, whereas it is unbounded in region II.

We will now discuss the symmetry-breaking patterns. These can be directly read from the vacuum configurations as follows.

For $\lambda_2 < 0$, V is minimized when there is only one nonzero ρ_a, which leads to the following form of the vacuum configuration:

$$\langle S_{Aa} \rangle = \rho \delta_{A1} \delta_{a1}. \tag{3.13}$$

The corresponding symmetry-breaking pattern is

$$SU(N_c) \times U(N_s) \to SU(N_c - 1) \times U(N_s - 1) \times U(1). \tag{3.14}$$

For $\lambda_2 > 0$, V is minimized when there are N_s nonzero ρ_a, providing

$$\langle S_{Aa} \rangle = \rho \delta_{Aa}. \tag{3.15}$$

In this case, the symmetry-breaking pattern is

$$SU(N_c) \times U(N_s) \to SU(N_c - N_s) \times SU(N_s) \times U(1). \tag{3.16}$$

These symmetry-breaking patterns are worked out in detail in Appendix F.

This concludes the tree-level analysis, naturally leading to the question as to whether or not higher orders can affect these findings. This will be discussed momentarily.

B. Quantum corrections

At the quantum level, there are two interesting cases classified according to how quartic coupling λ scaling with gauge coupling α.

(i) The Gildener Weinberg case [39]: λ scale linearly with α (i.e. $\lambda \sim \alpha$)
(ii) Alternative symmetry-breaking case (main focus in this section): λ scale with α^2 (i.e.$\lambda \sim \alpha^2$)

The Gildener Weinberg case works where the scalar couplings λ_i scale linearly with α (i.e. $\lambda \sim \alpha$). In this region, the classical (tree-level) symmetry-breaking lines Eq. (3.11) or (3.12) derived in the previous section remains intact. This is because quantum corrections will provide extra term $\sim\alpha^2$ in the tree-level lines Eq. (3.11) or (3.12) which is negligible since we are studying in the region $\alpha \ll 1$ and thus $\alpha^2 \ll \lambda$. In Gildener Weinberg case, the curvature of the effective potential generally will be proportional to $\lambda \sim \alpha$ and we need to choose a flat direction (to make curvature $\sim\alpha^2$), along which quantum corrections can induce radiative symmetry breaking when the RG flows cross the lines Eq. (3.11) or (3.12).

At the quantum level, interesting possibilities for the vacuum structure of the model may emerge when scalar and gauge couplings start competing (i.e. $\lambda_i \sim \alpha^2$). As it can be seen from the UV picture in Fig. 2, there are UV free trajectories which run arbitrarily close to the origin in (λ_1, λ_2)-space (indicated by a black dot), where the condition for the second case $\lambda_i \sim \alpha^2$ holds. In these cases, the tree-level potential is approximately flat in all directions, and the symmetry breaking is dominated by the gauge loop contributions. The symmetry breaking is therefore no longer restricted to the symmetry-breaking patterns discussed in the previous section. This possibility was first pointed out in [40] and we will explore the possibilities of alternative symmetry-breaking patterns by using RG improvement in the following. This scenario is phenomenologically interesting, since when all directions are flat, the model could radiatively generate a spectrum for all the scalar masses (see e.g. [50–52]), as compared to the Gildener-Weinberg scenario [39], where the only radiatively generated scalar mass is the mass of the scalon.

There are two main ways to implement the one-loop effects: explicit logarithmic summation (see e.g. [51–54]) or implicit logarithmic summation (see e.g. [55]). In this work, we focus mainly on the method of implicit RG improvement because the explicit calculations shown in Appendix H require diagonalization of the mass matrices which quickly becomes impractical for $N_c \geq 4$, $N_s \geq 3$ in the fundamental representation. The RG improvement method developed in this section could be generalized to arbitrary symmetry groups and representations.

The renormalization group improved effective potential is:

$$V(\{\rho_i\}) = \left[\lambda_1(t)\left(\sum_{i=1}^{N_s} \rho_i^2\right)^2 + \lambda_2(t) \sum_{i=1}^{N_s} \rho_i^4\right] \times \exp\left(4 \int_0^t dt' \gamma(t')\right), \tag{3.17}$$

where t is defined as $t = \log\left[\sum_{i=1}^{N_s} \rho_i^2/\mu^2\right]$ with renormalization scale μ and $\gamma(t)$ is the anomalous dimension of the scalar field. The model at hand generally does not allow for a Yukawa coupling, and therefore the anomalous dimension $\gamma(t)$ will, at one-loop level, be of order α. In the case where $\lambda(t) \sim \alpha^2$, the anomalous dimension will give rise to terms of the form $\lambda(t)\gamma(t) \sim \alpha^3$ in the minimization condition which can be regarded as higher-order effects. We can therefore further simplify the RG improved effective potential, Eq. (3.17), to

$$V(\{\rho_i\}) = \lambda_1(t)\left(\sum_{i=1}^{N_s}\rho_i^2\right)^2 + \lambda_2(t)\sum_{i=1}^{N_s}\rho_i^4 \equiv \lambda_1(t) f_1(\rho_i) + \lambda_2(t) f_2(\rho_i), \tag{3.18}$$

where we introduced functions f_1 and f_2 for convenience.

The RG improved minimization condition is given by:

$$V^{(1)}_{\rho_i} \equiv \frac{\partial V}{\partial \rho_i} = \sum_{j=1}^{2}\left(\frac{d\lambda_j}{dt}\frac{\partial t}{\partial \rho_i} f_j + \lambda_j \frac{\partial f_j}{\partial \rho_i}\right) = \sum_{j=1}^{2}\left(\beta_{\lambda_j}\frac{\partial t}{\partial \rho_i} f_j + \lambda_j \frac{\partial f_j}{\partial \rho_i}\right). \tag{3.19}$$

Now it is clear that although the effective potential is of the form of the tree level potential, the one-loop information is encoded through the RG functions $(\beta_{\lambda_1}, \beta_{\lambda_2})$.

In order for alternative vacuum configurations to exist, we need a number of distinct values of ρ_i to satisfy Eq. (3.19), which is different from the tree level assignments of ρ_i [i.e. Eqs. (3.13) and (3.15)]. For each distinct nonzero value of ρ_i, the minimization condition corresponds to a nontrivial constraint on the couplings. Since we have three marginal couplings $(\alpha, \lambda_1, \lambda_2)$, we therefore expect that at most there could be two distinct vacuum expectation values to fully determine symmetry-breaking lines in $(\alpha, \lambda_1, \lambda_2)$-space. In the case with three distinct vacuum expectation values, all three couplings will be fully determined and the system is already overdetermined. An exception to this is when $\lambda_2 = 0$; then there is only a single constraint on the remaining couplings which depends on f_1 and f_2.

We assume in the following that the vacuum configuration to be such that n_1 values of ρ_i are ρ, n_2 are $\kappa\rho$, with κ positive and different from unity, and $N_s - n_1 - n_2$ values equal to zero. From Eq. (3.19), we get two constraints on the couplings.

By solving Eq. (3.19), we obtain $\lambda_2 = 0$ at the broken scale. In this special case, the boundary sheets between the unbroken phase and broken phases become boundary lines; for each κ, this corresponds to a particular curve on the (λ_1, α) plane. It seems we could have alternative vacuum configurations and symmetry-breaking patterns since κ could be any non-negative value. As we explore further, we find in this case one of the eigenvalues of the mass matrix will always be negative, violating the vacuum stability conditions discussed below. Hence the alternative symmetry-breaking patterns scenario yields unphysical solutions.

Furthermore, the effective potential needs to be stable at the vacuum configuration, we therefore derive the eigenvalues of the Hessian matrix

$$V^{(2)}_{\rho_i\rho_j} \equiv \left.\frac{\partial^2 V}{\partial\rho_i\partial\rho_j}\right|_{\text{vacuum}}, \tag{3.20}$$

where all three RG functions $(\beta_{\lambda_1}, \beta_{\lambda_2}, \beta_\alpha)$ are encoded. A stable vacuum and physical scalar masses requires the eigenvalues to be non-negative.

We find that these requirements cannot be met [two distinct VEVs will always lead to one negative mass eigenvalue throughout Eq. (3.20)] unless $n_2 = 0$, and n_1 is either 1 or N_s. These are exactly the tree level vacuum configurations, implying no alternative symmetry-breaking patterns are found in this model beyond the two discussed at the tree level analysis, i.e. Eq. (3.14) and Eq. (3.16).

In Appendix G, we carry out the analysis of the case with $(N_c = 6, N_s = 3, N_f = 31)$. We find that the RG improved boundary lines (G3) and (G5) for the broken phases actually shift the tree level boundary lines when $\lambda_i \sim \alpha^2 \ll 1$. While, when $\lambda_i \sim \alpha \ll 1$ the RG improved reduces to the tree level result. In this way, Fig. 14 provides a detailed view of region near the origin of Fig. 7.

Similarly, in Appendix H, we perform the same analysis based on the explicitly calculated one-loop effective potential in the Coleman-Weinberg renormalization scheme. There are differences in the exact conditions on the couplings for spontaneous symmetry breaking, but the corresponding vacuum configurations, and thus symmetry-breaking patterns, are identical and the regions satisfying the vacuum stability conditions (comparing Fig. 16 with Fig. 12) are similar and consistent in both renormalization schemes.

IV. SUMMARY

We have simultaneously carried out a detailed study of the UV behavior and a classification of the IR phases of $SU(N_c)$ gauge theories with N_s complex scalars and N_f vector-like fermions in the fundamental representation.

This entailed a careful analysis of the conditions for complete asymptotic freedom (CAF). Interestingly, due to the presence of fundamental scalars, CAF requires a large number of colors, N_c, and a large number of fermions. We find for specific combinations of N_c and N_s a window in N_f for which the CAF conditions are satisfied. The most minimal case is $N_c = 5$ with $N_s = 2$. The CAF allowed number of fermions, N_f, is found to be close to the loss of

asymptotic freedom in the gauge beta function. We show that the CAF conditions are, remarkably, more restrictive than the requirement for the model to have IR fixed points, when considering higher orders. This means that any CAF model of this kind displays long distance conformality, at least in some coupling direction. We stress that our results are within perturbative control.

When considering the infrared fate of the model, we discover two distinct phase structures. For most combinations of N_c, N_f and N_s we have two IR fixed points, while for larger values of N_c and N_f with N_s small, four IR fixed points exist. For the models featuring two IR fixed points, neither of them are fully IR attractive and furthermore they reside on the separatrix between two radiatively broken phases. However for models featuring the four IR fixed points we observe that a fully IR attractive fixed point appears allowing for a stable phase of long distance conformality.

To investigate the possible existence of radiative symmetry breaking, we performed analyses both at tree- and one-loop levels. For the tree-level analysis, we used the conventional Gildener-Weinberg method, while at the quantum level, we used the renormalization group improved effective potential. The same two symmetry-breaking patterns were found for both analyses: $SU(N_c) \times U(N_s) \to SU(N_s) \times SU(N_c - N_s) \times U(1)$ and $SU(N_c) \times U(N_s) \to SU(N_c - 1) \times U(N_s - 1) \times U(1)$. This is despite the fact that the loop-level analysis allows one to study regions of phase space, where quantum corrections are dominating the vacuum configuration of the scalar fields.

Our analysis has shed light on the UV behavior and rich low energy phase structure of minimal extensions of QCD-like models featuring scalar quarks. We discovered that ensuring these models to be fully asymptotically free is related to the presence of long-distance conformality. Our results can be useful when constructing extensions of the standard model featuring vector-like dynamics.

ACKNOWLEDGMENTS

This work is partially supported by the Danish National Research Foundation under Grant No. DNRF:90. T. G. S. and R. B. M. are grateful for financial support from the Natural Sciences and Engineering Research Council of Canada (NSERC). Z. W. Wang thanks Matin Mojaza and Esben Molgaard for helpful discussions.

APPENDIX A: DIFFERENT APPROACHES TO COMPLETE ASYMPTOTIC FREEDOM

There are several seemingly different requirements to ensure that complete asymptotic freedom exists. In fact, they are all equivalent approaches for finding fixed flow relations among the couplings. In Sec. II A, we impose Eq. (2.4), which reads

$$(\beta_\alpha, \beta_{\lambda_1}, \beta_{\lambda_2}) = c(\alpha, \lambda_1, \lambda_2), \tag{A1}$$

where c is a scale-dependent quantity. If this requirement is satisfied and the system is well approximated by the one-loop beta functions, then this relation among the couplings will remain constant; in other words, the flow is fixed.

Another approach [9] is to factor out the known high-energy logarithmic scaling of the gauge coupling from all the three marginal couplings, i.e.

$$\alpha = \frac{\tilde{\alpha}}{t}, \qquad \lambda_1 = \frac{\tilde{\lambda}_1}{t}, \qquad \lambda_2 = \frac{\tilde{\lambda}_2}{t}, \tag{A2}$$

where $t = \log(\mu^2/\mu_0^2)$ and look for solutions where the parameters $\tilde{\alpha}$, $\tilde{\lambda}_1$ and $\tilde{\lambda}_2$ become constant for large t, i.e. fixed flows. This can be stated as

$$\begin{aligned} \frac{d\tilde{\alpha}}{d\log t} &= \tilde{\alpha} + \beta_\alpha(\tilde{\alpha}) = 0, \\ \frac{d\tilde{\lambda}_i}{d\log t} &= \tilde{\lambda}_i + \beta_{\lambda_i}(\tilde{\lambda}_i, \tilde{\alpha}) = 0 \quad (i = 1, 2), \end{aligned} \tag{A3}$$

where $\beta_\alpha(\tilde{\alpha})$ and $\beta_{\lambda_i}(\tilde{\lambda}_i, \tilde{\alpha})$ are the one-loop beta functions Eq. (2.2) with couplings replaced by $\tilde{\alpha}$, $\tilde{\lambda}_1$ and $\tilde{\lambda}_2$. The system Eq. (A3) is equivalent to Eq. (A1); however, this choice of parametrization conveniently fixes $c = -1$.

A related approach (see e.g. [56,57]) is to study the gauge coupling α together with the ratios $\lambda_{is} = \lambda_i/\alpha$ for $i = 1, 2$. CAF can be formulated as asymptotic freedom for the gauge coupling ($B > 0$) together with at least one fixed point in the subsystem ($\beta_{\lambda_{1s}}$, $\beta_{\lambda_{2s}}$). The benefit of this approach is that $\beta_{\lambda_{is}}/\alpha$ are functions only of λ_{1s} and λ_{2s}. However, we can write

$$\alpha^{-1}\beta_{\lambda_{1s}} = \alpha^{-2}\left(\beta_{\lambda_i} - \frac{\lambda_i}{\alpha}\beta_\alpha\right) = 0, \tag{A4}$$

which for large t can be stated in terms of the parameters Eq. (A2) as

$$\tilde{\alpha}^{-2}\left(\beta_{\lambda_i}(\tilde{\lambda}_i, \tilde{\alpha}) - \frac{\tilde{\lambda}_i}{\tilde{\alpha}}\beta_\alpha(\tilde{\alpha})\right) = 0. \tag{A5}$$

Imposing $\tilde{\alpha} + \beta_\alpha(\tilde{\alpha}) = 0$ ($B > 0$), we see that this reduces to the remaining equations of Eq. (A3). In the following section, we use the same method to ultimately reduce Eq. (A3) to a single quartic polynomial in λ_{2s}.

Similarly, one can study the ratios of beta functions, as in [11]. In this case, the fixed flow condition becomes $\beta_{\lambda_1}/\beta_\alpha = \lambda_i/\alpha$, which is equivalent to Eq. (A4).

APPENDIX B: QUARTIC POLYNOMIAL AND CLASSIFICATION OF ITS ROOTS

Here we provide the details for the procedure outlined in Sec. II A of reducing the fixed flow equation (2.4) to a quartic equation in a single coupling, λ_2. We will use the discriminant method to classify the roots of the equation.

We want to find solutions to

$$(\beta_\alpha, \beta_1, \beta_2) = c(\alpha, \lambda_1, \lambda_2), \tag{B1}$$

in the case where $c < 0$ and the beta functions are given by Eq. (2.2). First we note that β_α is only a function of α itself. We can, therefore, find the fixed flow solution for $\alpha \neq 0$ must satisfy $c = -B\alpha$, where $B = \frac{1}{3}(22N_c - 4N_f - N_s)$. Clearly, the condition $c < 0$ is only satisfied when $B > 0$. We can now substitute $c = -B\alpha$ into the remaining components of Eq. (B1). For $\alpha \neq 0$ it is convenient to introduce the rescaled couplings, $\lambda_i = \lambda_{is}\alpha$, for which we can factor out the gauge coupling dependence of the last two components of Eq. (B1). In other words, the two equations, $\alpha^{-2}(\beta_i - c\lambda_i) = 0$, can be written as

$$\begin{aligned}
&4(N_cN_s+4)\lambda_{1s}^2 + 12\lambda_{2s}^2 \\
&\quad + \lambda_{1s}\left[8(N_c+N_s)\lambda_{2s} + B - \frac{6(N_c^2-1)}{N_c}\right] + \frac{3(N_c^2+2)}{4N_c^2} = 0, \\
&4(N_c+N_s)\lambda_{2s}^2 + \lambda_{2s}\left[24\lambda_{1s} + B - \frac{6(N_c^2-1)}{N_c}\right] \\
&\quad + \frac{3(N_c^2-4)}{4N_c} = 0.
\end{aligned} \tag{B2}$$

In the case, where $B = 0$, the equations above no longer describe solutions to Eq. (B1), instead they correspond to the equations $\beta_i = 0$ for constant $\alpha \neq 0$. These solutions we refer to as fixed points in the quartic couplings subsystem, since in general the gauge coupling is not fixed.

Now, for $B > 0$, we can solve the second equation in Eq. (B2) for λ_{1s} and substitute into the first in order to obtain a quartic polynomial in λ_{2s} (after multiplying with λ_{2s}^2)

$$a\lambda_{2s}^4 + b\lambda_{2s}^3 + c\lambda_{2s}^2 + d\lambda_{2s} + e = 0, \tag{B3}$$

where

$$\begin{aligned}
9a &= N_s(N_s(2N_c^2 + N_cN_s - 8) + (N_c-4)N_c(N_c+4)) - 8N_c^2 + 108, \\
18N_cb &= (N_c(B-6N_c)+6)(N_s+N_c)(N_cN_s-5), \\
144N_c^2c &= 144 - 2N_c(B^2N_c - 12B(N_c^2-1) + 6N_c(7N_c^2-25)) \\
&\quad + N_cN_s((B^2-108)N_c^2 - 12BN_c^3 + 12BN_c + 42N_c^4 + 6(N_c^2-4)N_cN_s + 84), \\
96N_c^2d &= (N_c^2-4)(N_c(B-6N_c)+6)(N_cN_s+1), \\
256N_c^2e &= (N_c^2-4)^2(N_cN_s+4).
\end{aligned} \tag{B4}$$

In Sec. II A, we define the critical number of fermions, N_f^*, for which $B = 0$. Then defining $N_x = N_f^* - N_f$, we can express $B = 4N_x/3$. Following Ref. [58], the nature of the roots of a quartic equation of the form Eq. (B3) is described by the following functions

$$\begin{aligned}
\Delta &= 256a^3e^3 - 192a^2bde^2 - 128a^2c^2e^2 + 144a^2cd^2e - 27a^2d^4 + 144ab^2ce^2 - 6ab^2d^2e - 80abc^2de \\
&\quad + 18abcd^3 + 16ac^4e - 4ac^3d^2 - 27b^4e^2 + 18b^3cde - 4b^3d^3 - 4b^2c^3e + b^2c^2d^2 \\
P &= 8ac - 3b^2 \\
Q &= b^3 + 8da^2 - 4abc \\
\Delta_0 &= c^2 - 3bd + 12ae \\
D &= 64a^3e - 16a^2c^2 + 16ab^2c - 16a^2bd - 3b^4
\end{aligned} \tag{B5}$$

Since we are interested in real roots, we have the following relevant cases:

(i) If $\Delta < 0$, then the equation has two distinct real roots.

(ii) If $\Delta < 0$, while $P < 0$ and $D < 0$, then all four roots are real and distinct.

(iii) If $\Delta = 0$, then the equation has a multiple root and several scenarios exist.

Only when $D = 0$, $P > 0$, and $Q = 0$ are none of the roots real.

In Fig. 1, we show the regions in N_c and N_s for $N_x \in \{0, 1, 2, 3, 4\}$. The upper region satisfies condition (i), the lower region satisfies condition (ii), while the borders satisfy the condition $\Delta = 0$. In the range $N_c \in [3, 20]$, $N_s \in [2, 20]$ and $N_x \in [0, 20]$, there are no integer solutions to the last condition.

APPENDIX C: CONNECTION BETWEEN FIXED FLOWS AND FIXED POINTS

In Sec. II, we found that the set of models that are CAF is a subset of the models with interacting IR fixed points. This result was based on a numerical study of the two-loop gauge beta function together with the one-loop beta functions for the quartic couplings. The same study with three-loop gauge beta function is done in Appendix D. However restricting to the two-loop gauge beta function, we know that the running of the gauge coupling is independent of the quartic couplings. Within this approximation and inspecting the gauge coupling in isolation, the statement above appears easy to disprove. Writing the gauge beta function as $\beta_\alpha = -B\alpha^2 + C\alpha^3$, the set of models with AF is characterized by satisfying the condition, $B > 0$, while the interacting IR fixed point is realized only when both $B > 0$ and $C > 0$. In other words, requiring the model to have an interacting IR fixed point is a stronger condition than for the gauge coupling to be AF. This is the well-known result from Caswell, Banks and Zaks [45,46].

Adding on top of this the beta functions for the quartic couplings, we know from Appendix B that the CAF condition reduces to $B > 0$ and at least a real solution to Eq. (B2), while the existence of an interacting IR fixed point requires at least a real solutions to Eq. (B2) with $B = 0$ (not a constraint on N_c, N_s and N_f) with at least one IR attractive direction. The direction towards the Gaussian fixed point will be IR attractive if $B > 0$ and $C > 0$. Clearly, our numerical findings in Sec. II can be restated as follows: the set of $\{N_c, N_s\}$ for which there are solutions to Eq. (B2) with $B > 0$ (constraint on N_f) is a subset of the set of $\{N_c, N_s\}$ for which there are solutions to Eq. (B2) with $B = 0$, and simultaneously the set $\{N_c, N_s, N_f\}$ satisfying the CAF conditions is a subset of the $\{N_c, N_s, N_f\}$ satisfying $C > 0$, such that the seemingly additional constraint is always implied.

The first inclusion was shown pictorially in Fig. 1 for specific choices of N_f close to N_f^*. In the following, we will discuss this relation further and investigate the last inclusion in more depth.

Clearly, $B > 0$ is a common condition for both sets, while the CAF condition takes the form Eq. (B2), the existence of fixed points in λ_1 and λ_2 for $\alpha \neq 0$, are the solutions to $\alpha^{-2}\beta_i = 0$, which can be written as

$$\begin{aligned} &4(N_cN_s+4)\lambda_{1s}^2 + 12\lambda_{2s}^2 + \lambda_{1s}\left[8(N_c+N_s)\lambda_{2s} - \frac{6(N_c^2-1)}{N}\right] \\ &\quad + \frac{3(N_c^2+2)}{4N_c^2} = 0, \\ &4(N_c+N_s)\lambda_{2s}^2 + \lambda_{2s}\left[24\lambda_{1s} - \frac{6(N_c^2-1)}{N_c}\right] + \frac{3(N_c^2-4)}{4N_c} = 0, \end{aligned} \tag{C1}$$

in rescaled couplings. Notice, that this equation is equivalent to Eq. (B2) without the B-terms. However, this derives from the fact that fixed points are solutions to $\beta_i = 0$, while fixed flows are solutions to $\beta_i = -B\alpha\lambda_i$. In other words, $B = 0$ is not a constraint for the fixed point equation, but a limit in which Eq. (B2) reduces to Eq. (C1).

It is not an easy task to show that the set of $\{N_c, N_s\}$ with real solutions to Eq. (C1) is bigger than for Eq. (B2) with $B > 0$. However, we can make some simple observations. Consider only solutions where both λ_1 and λ_2 are positive. Then since both equations, evaluated at $\lambda_{is} = 0$, are positive for $N_c > 2$, it is clear that there have to be a solution to $\beta_i = 0$ before there can be a solution to $\beta_i = -B\alpha\lambda_i$, since the latter are negative. For the cases where one or both of the two λ_{is}'s are negative, this reasoning does not hold. By demanding a stable scalar potential, the case where both λ_1 and λ_2 are negative can be discarded. In this way, we are left with the cases with one of the quartic couplings being negative. Here we do not need to cross $\beta_i = 0$ for both beta functions to satisfy $\beta_i = -B\alpha\lambda_i$ and for general coefficients of Eq. (B2), this can be realized. However, for the particular N_c and N_s dependence of the coefficients for this model, it is not the case. For $0 \leq N_f^* - N_f < 8/\sqrt{3}$, the coefficient C is always positive. For $N_f^* - N_f \geq 8/\sqrt{3}$, the sign of C depends on the N_c and N_s. However, since $C > 0$ for large values of N_c, even when $N_s \sim N_c$, and C is a continuous function in N_c, N_s and N_f, we can solve for N_f in $C = 0$, and check for real solutions to Eq. (B2). Using the same method described in Appendix B, we find no real solutions with $C = 0$; we conclude, since we know that the region with real solutions is connected, that $C > 0$ for all obtained solutions. In Fig. 8, we illustrate this fact by plotting the lower value of N_c (blue line), as a function of N_x, above which there are solutions, together with the value of N_c (red line) below which $C < 0$ for $N_s = 1$. The two lines never intersect, and this supports the statement, that $C > 0$ in the whole region of solutions to Eq. (B2).

We will now present the morphology of the phase diagram of the rescaled beta functions given by the left sides of Eq. (C1). A study of the curves, where each one of the two beta functions is zero, leads to the conclusion, that in the region where the two distinct real roots exist, both roots will be positive and the phase diagram looks schematically like shown (dashed gray) in left panel Fig. 9. In the dark gray region of Fig. 1, two roots are similar to the previous case and still positive, while the two additional roots in λ_{2s} are positive, but larger, and paired with negative values of λ_{1s}. The corresponding phase diagram is shown (dashed gray) in the right panel of Fig. 9. The fixed points (gray dots) are solutions to Eq. (C1) where the gauge dependence is factored out. The relation to the actual couplings is $\lambda_i = \lambda_{is}\alpha$, and the position of these points will therefore move unless the gauge coupling has a nontrivial fixed point. For models with CAF, we already

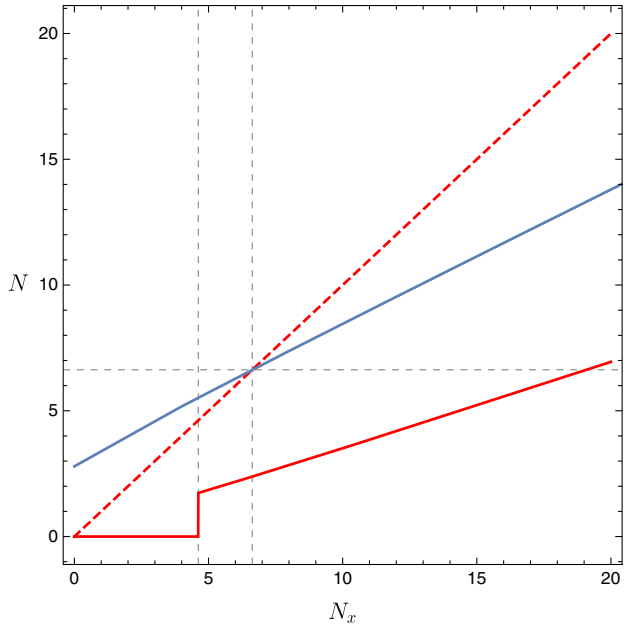

FIG. 8. The blue line marks the lower value of N_c, as a function of N_x, above which there are solutions to Eq. (B2). The red solid line is the value of N_c for which the curve, $C = 0$, intersects $N_s = 1$. Below this line there is a region with $N_s \geq 1$ for which $C < 0$. For $N_x < 8/\sqrt{3}$ the curve with $C = 0$ does not intersect $N_s = 1$ (marked with gray dashed line). The dashed red line is straight line $N_c = N_x$ below which the suppression of higher-loop contributions to the IR fixed points are of order one.

know that there exists interacting IR fixed points, $\alpha^* = B/C$.

In the UV, the gauge coupling is AF and the solutions in λ_{is} are fixed flows which all go to zero. If we require the quartic couplings also to be AF, they need to be fixed in this geometrical rescaling along the fixed flows. Possible candidates are the points where the flow is pointing towards the origin, i.e. $(\beta_{\lambda_1}, \beta_{\lambda_2}) = c(\lambda_1, \lambda_2)$ with $c < 0$, i.e. the last two equations in Eq. (2.4). Factoring out the gauge coupling, the condition becomes

$$\alpha^{-2}(\beta_1, \beta_2) = c_s(\lambda_{1s}, \lambda_{2s}) \tag{C2}$$

where $c_s = c/\alpha$. When $c_s = -B$, this equation equals Eq. (B2). Solving the equation for $c_s < 0$ gives the blue solid lines in Fig. 9, whereas the solutions for $c_s > 0$ are shown as dashed red lines.

In order to leave the geometry in λ_{1s} and λ_{2s} unchanged, the magnitude of the flow needs to match the change in the gauge coupling, α, i.e. corresponding to a uniform contraction:

$$(\beta_\alpha, \beta_{\lambda_1}, \beta_{\lambda_2}) = c(\alpha, \lambda_1, \lambda_2). \tag{C3}$$

This condition is the fixed flow equations Eq. (2.4) for the gauge and quartic couplings introduced in Sec. II A. Here we showed that $c = -B\alpha$. This means that the solutions to the CAF condition are specific points along the blue curves. In Fig. 10, we plot the rescaled beta function, $\beta_{2s} = \alpha^{-2}\beta_2$, for λ_2 along the line given by Eq. (C2) parametrized by λ_{1s}. In the same picture, we superimpose the condition $c\lambda_2$ for $c < 0$. From this plot, we see the relation between the fixed flow solutions (blue dots) and the fixed points in the quartic subsystem (gray dots). Furthermore, we see why they come in pairs, and since we assume the shape to be characteristic for the whole solution space, we understand why we always have fixed points in the quartic subsystem when we have fixed flow solutions.

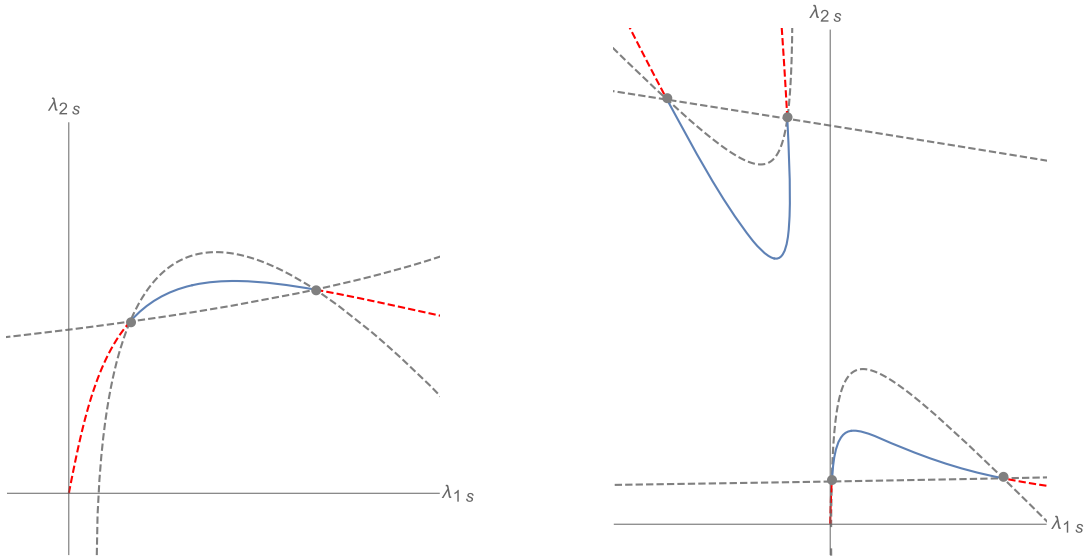

FIG. 9. Morphology of the quartic phase diagram. Each gray dashed curve represent the zero-contour of one of the rescaled quartic beta functions. The blue solid lines (red dashed lines) mark the curves where the flow is pointing towards (away from) the origin. The grey dots are the fixed points in the quartic subsystem. Right: For the case of two solutions. Left: For the case of four solutions.

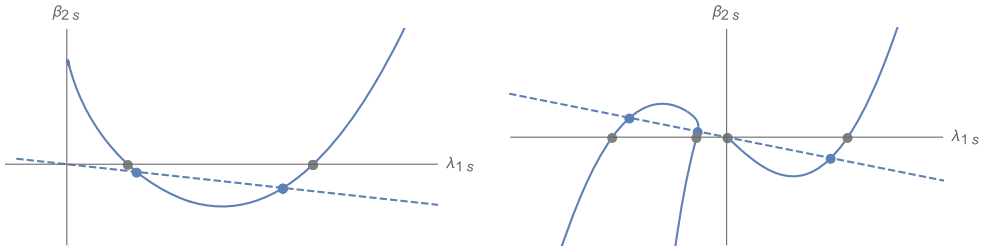

FIG. 10. This shows the corresponding beta function of the flows along the lines shown in Fig. 9, parametrized by λ_{1s}. The dashed line is where the $c_s = 2B$. The grey dots are the fixed points in the quartic subsystem, and the blue dots are solutions to the fixed flow. Right: For the case of two solutions. Left: For the case of four solutions.

APPENDIX D: THREE-LOOP GAUGE CONTRIBUTION ANALYSIS

As discussed in Sec. II B, for a Weyl-consistent approach we would have to include the three-loop correction to the gauge renormalization group equation in our IR analysis. This takes the form

$$\begin{aligned}\beta_\alpha^{(3)} = {} & (-2N_s\lambda_1^2 - 2N_cN_s^2\lambda_1^2 - 4N_cN_s\lambda_1\lambda_2 - 4N_s^2\lambda_1\lambda_2 - 2N_s\lambda_2^2 - 2N_cN_s^2\lambda_2^2)\alpha^2 \\ & + \left(N_cN_s\lambda_1 - \frac{2N_s\lambda_1}{N_c} + 2N_s^2\lambda_1 + 2N_s\lambda_2 - \frac{2N_s^2\lambda_2}{N_c} + N_cN_s^2\lambda_2\right)\alpha^3 \\ & + \left(\frac{1709N_c^2N_f}{27} - \frac{2857N_c^3}{27} - \frac{187N_f}{18} - \frac{N_f}{2N_c^2} + \frac{11N_f^2}{9N_c} - \frac{102N_cN_f^2}{27} - \frac{1651N_s}{77}\right. \\ & \left. + \frac{29N_s}{8N_c^2} + \frac{1315N_c^2N_s}{56} + \frac{73N_fN_s}{36N_c} - \frac{335N_cN_fN_s}{108} + \frac{49N_s^2}{77N_c} - \frac{143N_cN_s^2}{216}\right)\alpha^4. \end{aligned} \tag{D1}$$

We notice that the gauge coupling is no longer decoupled from the quartic coupling system, which makes a similar approach to the one performed in Sec. II A unavailable. We can however say some general things about the structure of the beta function, which now takes the form $\beta_\alpha = -B'\alpha^2 + C'\alpha^3 + D\alpha^4$, where B' and C', unlike the case of the two-loop beta function, depend on the quartic couplings. Close to the Gaussian fixed point, following the reasoning of Sec. II A, the quartic couplings scale as $\lambda_i \propto \alpha \ll 1$, and the new terms in B' and C' become of order α^4, such that B' and C' in this limit become B and C from the two-loop case.

Similarly, we know from Appendix C that $\lambda_i^* = \lambda_{is}^*\alpha^*$, so as long as $\lambda_{is}^* \sim \mathcal{O}(1)$ and $\alpha^* \ll 1$, we obtain the same result that the dependence of the quartic couplings is moved to the D coefficient.

Here we will first argue that $\lambda_{is}^* \sim \mathcal{O}(1)$ or smaller, and then use this result to show that the three-loop contribution to α^* is sub leading in certain limits. Afterwards we will use a numerical approach to determine the IR fixed points and produce a table similar to Table III.

Studying the rescaled one-loop beta functions (left-hand side of Eq. (C1) in the large N_c and N_s, but fixed $N_s/N_c = k$, limit, we find the rescaled couplings to be roughly of the order (leading term)

$$\begin{aligned} \mathrm{FP}_1 &= \left\{\frac{3-\sqrt{9-3k}}{4k}\frac{1}{N_c}, \frac{3-\sqrt{6-3k}}{4(k+1)}\right\} \\ \mathrm{FP}_2 &= \left\{\frac{3+\sqrt{9-3k}}{4k}\frac{1}{N_c}, \frac{3-\sqrt{6-3k}}{4(k+1)}\right\} \\ \mathrm{FP}_3 = \mathrm{FP}_4 &= \left\{-\frac{\sqrt{3}(k+1)\sqrt{k(k^2-k+10)}+9k}{4(k^3-k^2+k)}\frac{1}{N_c}, \frac{3+\sqrt{6-3k}}{4(k+1)}\right\}, \end{aligned} \tag{D2}$$

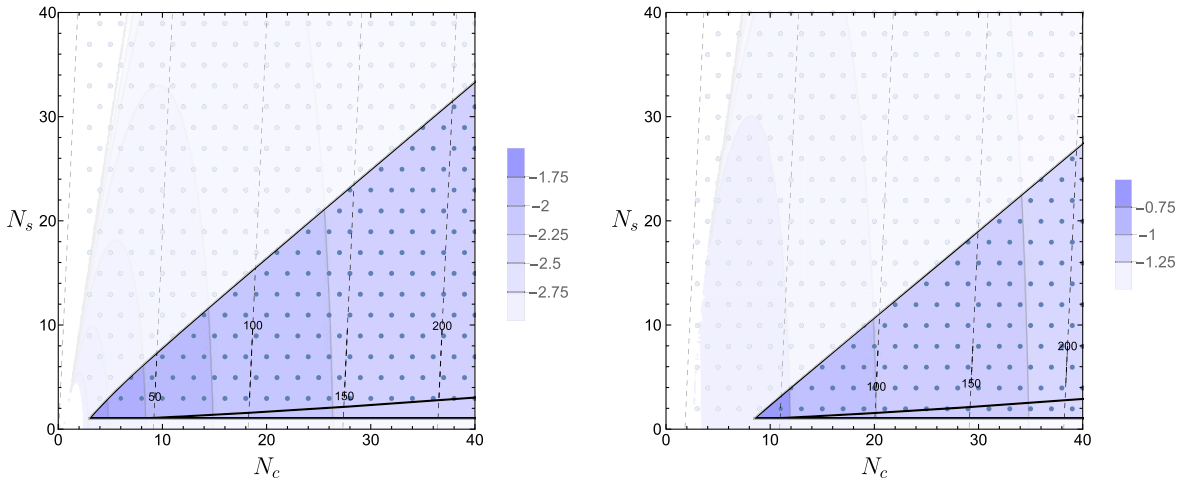

FIG. 11. Estimate of the relative size of the three-loop contribution. The dots mark integer values of N_c, N_s and N_f such that $N_x = 1/4$ in the left panel and $N_x = 10$ on the right. The excluded regions does not satisfy the CAF conditions. The dashed contours are values of N_f, while colored regions show the relative size of the three-loop contribution as $\log_{10}|\alpha_3^* - \alpha_2^*|/\alpha_2^*$, with α_2^* given by Eq. (D3), while α_3^* is the three-loop result assuming for simplicity that $\lambda_1 = \lambda_2 = \alpha$.

where the format is $\mathrm{FP}_i = \{\lambda_{1s}, \lambda_{2s}\}$, and FP_1, FP_2 are the two fixed points we have in regions with two solutions, while FP_3, FP_4 are the additional ones in the four solution region. The value of k is constrained from the slopes of the borders of the grey regions on Fig. 1, which means $k \in [0, 0.84]$. Notice, they all are of the order $\{\mathcal{O}(1/N_c), \mathcal{O}(1)\}$.

The fixed point at two-loop order is given by

$$\alpha_2^* = \frac{B}{C} = \frac{8N_xN_c}{150N_c^3 + N_c^2(3N_s - 52N_x) - 66N_c - 9N_s + 12N_x}, \tag{D3}$$

which in the same limit as taken above is

$$\alpha_2^* = \frac{8}{3(k+50)}\frac{N_x}{N_c^2} + \mathcal{O}\left(\frac{N_x^2}{N_c^3}\right) \tag{D4}$$

With these results at hand, we can determine the dominating terms in Eq. (D1). There are N^3 terms (counting N_c, N_s and N_f as N) coming from both B', C' and D, where the contributions from B' (C') depend quadratically (linearly) on λ_{2s}. However, when $\alpha^* \propto N_x/N_c^2$, these terms are suppressed by a factor of N_x/N_c and will thus only contribute to the sub leading terms of Eq. (D4). The degree of suppression can roughly be estimated by comparing the blue solid line with the dashed red line in Fig. 8. Assuming instead $\lambda_{1s} = \lambda_{2s} = 1$, we can easily calculate the size of the corrections. These are shown in Fig. 11 for $N_x = 1/4$ and $N_x = 10$, respectively.

Following the numerical approach to determine the existence of IR fixed points, by solving $(\beta_\alpha, \beta_1, \beta_2) = 0$, we the results in Table V.

As expected, when comparing Tables III and V we see that the upper boundary of the window in N_f remains unchanged when including the three-loop contribution to the gauge beta function. The lower boundary, however, is lowered. Furthermore, we find the existence of another lower limit of N_f which lies above the CAF solutions. For any value of N_f above this limit the system exhibits IR fixed points. These are not shown in the table.

TABLE V. Window in N_f that allow for perturbative IR fixed points for $N_s = \{2, 9\}$, $N_c = \{4, 12\}$, when including the three-loop contributions of the gauge coupling beta function. There are no solutions for $N_c = 3$ for $N_s > 1$.

	$N_c = 4$	$N_c = 5$	$N_c = 6$	$N_c = 7$	$N_c = 8$	$N_c = 9$	$N_c = 10$	$N_c = 11$	$N_c = 12$
$N_s = 2$	10–21	10–26	11–32	13–37	15–43	17–48	19–54	21–59	23–65
$N_s = 3$		10–26	11–32	13–37	15–43	17–48	19–54	21–59	22–65
$N_s = 4$			11–31	13–37	14–42	16–48	18–53	20–59	22–64
$N_s = 5$				12–37	14–42	16–48	18–53	20–59	22–64
$N_s = 6$					14–42	16–47	17–53	19–58	21–64
$N_s = 7$						15–47	17–53	19–58	21–64
$N_s = 8$								19–58	21–63
$N_s = 9$									20–63

APPENDIX E: DIAGONALIZATION OF S

We start by left-multiplying S by an appropriate $SU(N_c)$ matrix. To find it, note that an arbitrary unitary matrix satisfies the following two properties:

(i) Each row A satisfies $\sum_B |U_{AB}|^2 = 1$. This imposes a constraint on one degree of freedom for each row.
(ii) Each pair of columns (A,B) with $A \neq B$ satisfies $\sum_C U^*_{CA} U_{CB} = 0$. Each of these imposes a constraint on two degrees of freedom (one complex number).

Proceeding row-by-row, the first row has $2N_c - 1$ degrees of freedom (only the first constraint) and the nth row now has $2N_c - 2n + 1$ degrees of freedom (first constraint and $n-1$ second constraints). Now, this matrix multiples the $N_c \times N_s$ complex matrix. We can conclude that

(i) If $2N_c - 2n + 1 \geq 2N_s$, we have enough freedom to set all entries of the nth row of S to 0. Solving for n, we can conclude that we can set $N_c - N_s$ rows to 0.
(ii) For row numbers greater than $N_c - N_s$, we will have $2N_s - 2N_c + 2n - 1$ degrees of freedom remaining. Starting from $n = N_c - N_s + 1$, we will be left with 1,3,5,… degrees of freedom, which translates to one real number and 0,1,2,… complex numbers.

Having cast S into a triangular form, we can right-multiply it by an $SU(N_s)$ matrix and repeat the argument to arrive with matrix that is diagonal in one $N_s \times N_s$ block.

Decomposing D in terms of a vacuum expectation value part (Σ) and a diagonal perturbation (H), the field S can finally be written in the form

$$S = e^{i\pi_c^I(x) t_c^I / f_c} (\Sigma + H(x)) e^{-i\pi_s^J(x) t_s^J / f_s}. \tag{E1}$$

From the Σ term, we can find the combination of generators which do not leave the vacuum invariant, which will define our symmetry-breaking pattern. These generators will correspond to the Goldstone bosons. Note that the Goldstone fields corresponding to the color symmetry, π_c, can be set to zero by an appropriate choice of gauge (unitary gauge), in which some of the vector bosons become massive. The Goldstone fields corresponding to flavor symmetry on the other hand become real, massless degrees of freedom.

APPENDIX F: SYMMETRY BREAKING PATTERNS

In Sec. III A, we found from the tree-level analysis two possible vacuum configurations of the scalar fields.

For $\lambda_2 < 0$, the tree-level potential is minimized when there is only one nonzero vacuum expectations value of the scalar matrix, S, i.e.

$$\langle S_{Aa} \rangle = \rho \delta_{A1} \delta_{a1}. \tag{F1}$$

For $\lambda_2 > 0$, the potential is minimized when there is N_s nonzero elements, i.e.

$$\langle S_{Aa} \rangle = \rho \delta_{Aa}. \tag{F2}$$

In the following, we will derive the corresponding symmetry-breaking patterns. To do so, we return to Eq. (E1) and note first that canonical normalization of π fields requires $f_c = f_s = \sqrt{\rho}$ in both symmetry-breaking cases. We are looking for combinations of π_c^I and π_s^J, which leave the vacuum state invariant, in other words satisfy the relation

$$\pi_c^I(x) t_c^I \Sigma - \pi_s^J \Sigma t_s^J = 0. \tag{F3}$$

We will now consider both cases separately, starting with the $\Sigma_{Aa} = \rho \delta_{Aa}$ case. Assuming $N_c > N_s$, we can divide the total of $N_s^2 + N_c^2 - 1$ generators (including $N_c + N_s - 1$ diagonal ones) of $SU(N_c) \times U(N_s)$ into four different categories:

(1) All color generators, with nonzero entries when both indices are in range $N_s + 1, \ldots, N_c$ (total: $(N_c - N_s)^2 - 1$ out of which $N_c - N_s - 1$ are diagonal). These clearly satisfy (F3) with $\pi_s^J = 0$. These generators form an $SU(N_c - N_s)$ algebra.
(2) All color generators with nonzero entries when both indices are in $1, \ldots, N_s$ range and all flavor generators except identity (total $2N_s^2 - 2$ out of which $2N_s - 2$ are diagonal). In this case, we can choose the generators such that $t_c^I = t_s^I = t^I$, and noting that all t^I commute with Σ (because it is a diagonal matrix), we can write (F3) as

$$(\pi_c^I - \pi_s^I) t^I = 0, \tag{F4}$$

which implies that $\pi_c^I = \pi_s^I$ by linear independence of SU(N) generators. This implies that there are $N_s^2 - 1$ unbroken generators when $\pi_c^I = \pi_s^J$, which form an algebra of $SU(N_s)$ and $N_s^2 - 1$ broken generators.
(3) Remaining diagonal generators (total: 2). These are the identity matrix of $U(N_s)$ and one matrix from the Cartan subalgebra of $SU(N_c)$, which we will call t^0. We require $\mathrm{Tr} t^0 t_c^I = 0$ for all $a \neq 0$ and in particular for all the diagonal Cartan subalgebra generators. But we have already considered above all the generators which form an $SU(N_s)$ Cartan subalgebra on the first N_s entries and are zero on the remaining ones and all the generators that form a Cartan subalgebra on the last $N_c - N_s$ entries and are zero in the first N_s entries. The only way the trace condition can be satisfied is if t^0 is separately proportional to the identity matrix on the first N_s entries and on the last $N_c - N_s$ entries, with proportionality constants chosen in such a way that it is traceless (as required by the algebra of $SU(N_c)$). But the fact that the matrix is proportional to the identity

on the first N_s entries implies that $t^0\Sigma \propto \Sigma$ and we can choose the coefficient π_c^0 together with the coefficient of the identity matrix in flavor space in such a way that the symmetry is unbroken. As a consequence, we have one unbroken generator, which corresponds to the $U(1)$ symmetry, while the other generator is broken.

(4) The next type of generator we will consider are off-diagonal generators with nonzero entries where one index is in $(1\ldots N_s)$ range and the other is in $(N_s+1,\ldots N_c)$ range $(2(N_c-N_s)N_s$ total). These will necessarily break the vacuum, because the second term of Eq. (F3) would need to transform a row of zeroes into one containing a ρ.

We have thus classified all the generators of $SU(N_c)\times U(N_s)$ and conclude that the symmetry-breaking pattern corresponding to vacuum 1 is

$$SU(N_c)\times U(N_s) \to SU(N_c-N_s)\times SU(N_s)\times U(1). \tag{F5}$$

The other symmetry-breaking pattern has the vacuum configuration which is zero everywhere except for the (1,1) entry. We again discuss the broken and unbroken generators by splitting $N_c^2+N_s^2-1$ generators into three different groups.

(1) All generators of $SU(N_c)$ and $U(N_s)$ with vanishing first row and column $((N_c-1)^2+(N_s-1)^2-1$ generators, including N_c+N_s-3 diagonal ones) These generators annihilate the vacuum by themselves and are therefore all unbroken. The corresponding symmetry subgroup is $SU(N_c-1)\times U(N_s-1)$.

(2) All off-diagonal generators with nonvanishing entries in the first row and column $(2(N_c+N_s-2)$ generators) The generators of $SU(N_c)$ will change the row in which ρ appears, while the generators of $SU(N_s)$ will change the column in which the ρ appears, so there is no combination, which will leave the vacuum invariant—all these generators are broken.

(3) Remaining diagonal generators (2 generators) The remaining generators are one $SU(N_c)$ generator and one $SU(N_s)$ generator, which are diagonal with nonzero first entry. This implies that the action of each of these generators on the vacuum will be proportional to the vacuum state, and we can tune the corresponding fields so that the symmetry generator corresponding to this linear combination vanishes, as before. We are therefore left with one broken generator and one unbroken generator, which corresponds to anouther $U(1)$ symmetry.

In conclusion, the symmetry-breaking pattern in this case is

$$SU(N_c)\times U(N_s) \to SU(N_c-1)\times U(N_s-1)\times U(1). \tag{F6}$$

APPENDIX G: RENORMALIZATION GROUP IMPROVED EFFECTIVE POTENTIAL

The formalism for studying spontaneous symmetry breakdown using the RG improved effective potential was introduced in Sec. III B. Here we will analyze the derived conditions for the case with ($N_c=6$, $N_s=3$, $N_f=31$).

We first focus on the case where $\kappa=1$, which corresponds to the case of Eq. (3.16) and plot the results in Fig. 12. We calculate the Hessian matrix using Eq. (3.20). The first two eigenvalues are degenerate and lead to the following constraint:

$$\lambda_2 \geq \frac{1}{16}(-17g^4-16\lambda_1), \tag{G1}$$

where we have already ignored the higher-order terms $\lambda_i^n(n\geq 2)$ and $g^m(m\geq 4)$ in the above expression. The above vacuum stable line is shown in red in Fig. 12. The third mass eigenvalue will lead to (again ignoring higher-order terms)

$$\lambda_2 \geq \frac{1}{16}(-119g^4-48\lambda_1) \tag{G2}$$

which is shown in green in Fig. 12. In addition, the RG improved boundary line will be given by Eq. (3.19) with respect to $k=1$, leading to

$$35g^2-240\lambda_1-2+\sqrt{-611g^4+13440g^2\lambda_1-140g^2+38592\lambda_1^2-768\lambda_1+4}=0, \tag{G3}$$

which is the blue line in Fig. 12.

We combine the above two vacuum stability lines with the RG improved boundary line for the broken phase in Fig. 12. It is very clear that when RG flows run into the shaded region (shown in blue), the symmetry is broken and we have the symmetry-breaking pattern: $SU(N_c)\times U(N_s)\to SU(N_c-N_s)\times SU(N_s)\times U(1)$.

We likewise plot in Fig. 13 the results for $\kappa=0$. In this case, the two degenerate mass eigenvalues and one nondegenerate mass eigenvalue provide the following two constraints

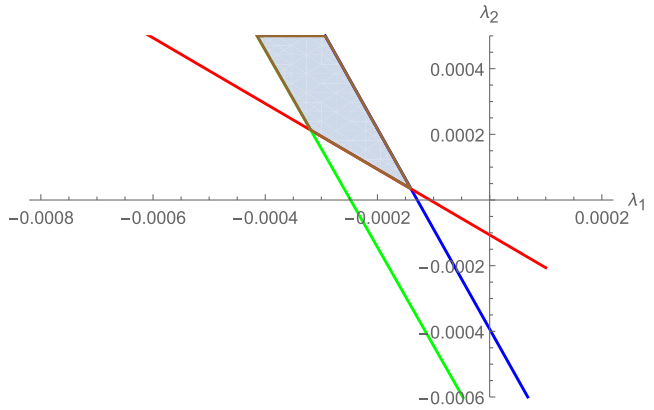

FIG. 12. In this figure, we choose a particular slice at $g = 0.1$ perpendicular to the gauge coupling direction. The blue line corresponds to the symmetry-breaking boundary line while the green and red lines come from two vacuum stability conditions. The blue shaded region represent the broken phase $SU(N_c) \times U(N_s) \to SU(N_c - N_s) \times SU(N_s) \times U(1)$.

$$\lambda_2 \geq \frac{1}{144}(-805g^4 - 144\lambda_1);$$
$$\lambda_2 \leq \frac{1}{96}\left(35g^2 - 96\lambda_1 - \sqrt{305g^4 + 4992\lambda_1^2 - 384\lambda_1}\right), \quad \text{(G4)}$$

which correspond to the purple and orange lines, respectively, in Fig. 13. Furthermore, by using Eq. (3.19) with respect to $\kappa = 0$, the RG improved boundary line for the broken phase ($\kappa = 0$) is

$$\lambda_2 \leq \frac{1}{96}\left(35g^2 - 96\lambda_1 - 2\sqrt{305g^4 - 140g^2 + 4992\lambda_1^2 + 4}\right) \quad \text{(G5)}$$

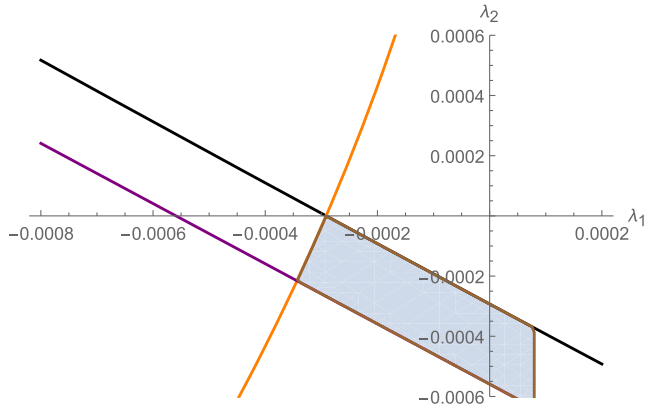

FIG. 13. In this figure, we choose a particular slice at $g = 0.1$ perpendicular to the gauge coupling direction. The black line corresponds to the symmetry-breaking boundary line while the orange and purple lines come from two vacuum stability conditions. The blue shaded region represent the broken phase $SU(N_c) \times U(N_s) \to SU(N_c - 1) \times U(N_s - 1) \times U(1)$.

and is shown in black in Fig. 13. The two vacuum stability lines and the RG improved boundary line for the broken phase (for $\kappa = 0$ case) are together illustrated in Fig. 13.

In Fig. 14, we combine the above two cases, with the two shaded regions representing the broken phases $SU(N_c) \times U(N_s) \to SU(N_c - N_s) \times SU(N_s) \times U(1)$ and $SU(N_c) \times U(N_s) \to SU(N_c - 1) \times U(N_s - 1) \times U(1)$, respectively. Note that Fig. 14 is consistent with the tree level diagram (Fig. 7) in the previous section. From the previous section, it is clear that the RG improved boundary lines (G3) and (G5) for the broken phases actually shift the tree level boundary lines slightly, as described in (3.11) and (3.12), at the origin of the coupling space (λ_1, λ_2). Magnification near the origin of Fig. 7 yields the detailed structure shown in Fig. 14. When scalar couplings are large the coarse grained picture in Fig. 7 emerges.

Combining the boundary lines for the broken phases and the vacuum stability lines with the RG flows yields Fig. 15. We have chosen the particular slice at $g = 0.044$ which is the coupling value of the Banks-Zaks fixed points. Note that the scalar quartic couplings have been rescaled to be compatible with the stream plot; the couplings on the axes are the rescaled couplings (with much larger values than the physical couplings).

The Banks Zaks fixed point shown in blue is fully repulsive in this slice and plays the role of an interacting UV fixed point (in this two-dimensional slice). It is very clear that there are RG flows running from this interacting UV fixed point (blue) towards the CP3 region (where $\lambda \sim O(g^n)(n \geq 4)$, shown in shaded blue). It is also clear that, in the two-dimensional slice, there are also RG flows running from interacting UV fixed point towards the Gildener Weinberg region (where $\lambda \sim O(g^2)$) of the broken

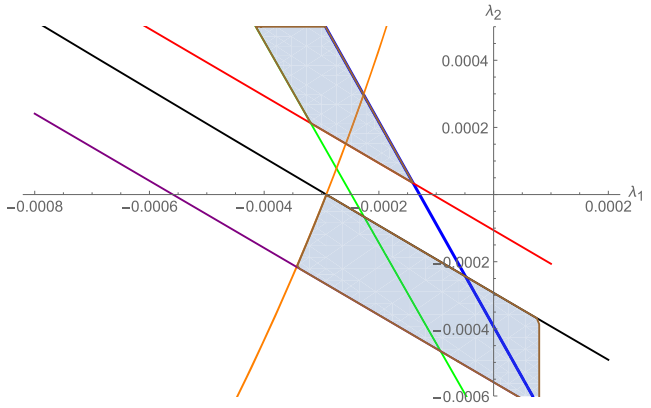

FIG. 14. In this figure, we choose a particular slice at $g = 0.1$ perpendicular to the gauge coupling direction. The blue and black lines correspond to the symmetry-breaking boundary lines while the orange, purple, red and green lines come from four vacumm stability conditions, respectively. The two shaded regions represent the broken phases $SU(N_c) \times U(N_s) \to SU(N_c - N_s) \times SU(N_s) \times U(1)$ and $SU(N_c) \times U(N_s) \to SU(N_c - 1) \times U(N_s - 1) \times U(1)$, respectively.

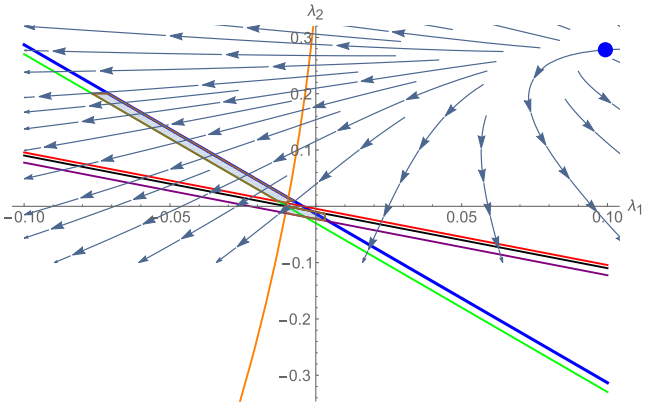

FIG. 15. In this figure, we choose a particular slice $g = 0.044$ which is the coupling value of the Banks-Zaks fixed points. The two shaded regions represent the broken phases $SU(N_c)\times U(N_s)\to SU(N_s)\times SU(N_c-N_s)\times U(1)$ and $SU(N_c)\times U(N_s)\to SU(N_c-1)\times U(N_s-1)\times U(1)$, respectively.

phase. Since there is no particular boundary between these two regions, we obtain phases with complete asymptotic safety in the UV (with perturbative couplings) and symmetry breaking in the IR regardless of whether scalar couplings scale with lower powers of the gauge coupling (Gildener-Weinberg) or higher (CP3). Furthermore, there are two attractive directions of the fixed point (one coming from the UV Gaussian fixed point and run into the plane (through back of the plane) the other one running into the plane through the front). Hence, there are some flows that do not come directly from the blue fixed point in this two-dimensional slice but run from the UV Gaussian fixed point, passing the IR fixed point and run towards the CP3 region. A similar conclusion holds for the Gildener Weinberg region. Thus there exist phases that are completely asymptotically free in the UV, symmetry breaking in the IR, and walking behavior in the middle regardless of whether scalar couplings scale with lower powers of the gauge coupling (Gildener-Weinberg) or higher (CP3). The symmetry breaking patterns are summarized in Table VI.

APPENDIX H: ONE-LOOP EFFECTIVE POTENTIAL

In Sec. III B, we used RG improvement to analyze the effective potential. This approach has several advantages:

(i) Loop-level contributions are already encoded in the RG functions. No explicit calculations of loop contributions to the effective potential are required.
(ii) No initial assumption about $\lambda \sim g^4$ is required. All orders of g are summed and already encoded.
(iii) Both gauge loop and scalar loop contributions are included.
(iv) It is much easier to generalize this approach to different symmetry groups and representations.

In this appendix, we sketch an explicit way to analyze the effective potential. To simplify the calculation, we study the $SU(3_c)\times U(3_s)$ case and assume the tree level contribution $O(\lambda)$ is comparable to the one-loop gauge contribution g^4 (i.e. $\lambda \sim g^4$), implying the next-order scalar contributions can be ignored ($\lambda^2 \sim g^8$). Explicit calculations are carried out in the Coleman-Weinberg scheme, which satisfies the Coleman-Weinberg renormalization conditions (discussed below) [38,40].

The one-loop effective potential is given by

$$V_{\text{eff}}^{\text{1loop}} = V_0 + V_g + V_{ct} \tag{H1}$$

where V_0, V_g, V_{ct} represent the tree level term, the gauge loop contribution and the counter-terms, respectively. The one-loop gauge contribution can be further written as [59]

$$V_g = \frac{3}{64\pi^2}\text{Tr}[M^4(\boldsymbol{S})\log M^2(\boldsymbol{S})], \tag{H2}$$

where $\boldsymbol{S}$ is the scalar field under fundamental representation of $SU(3_c)\times U(3_s)$ and

$$\begin{aligned} M^2_{IJ} &= g^2 t^I_{ji} t^J_{ik} S^{f\dagger}_j S^f_k = g^2 t^I_{ji} t^J_{ik} \boldsymbol{\chi_{jk}} \\ \boldsymbol{\chi_{jk}} &= \text{diag}(\rho_1^2, \rho_2^2, \rho_3^2) \quad (I, J = 1, \cdots 8). \end{aligned} \tag{H3}$$

The diagonalization of $\boldsymbol{S}$ is discussed in great detail below Eq. (3.2). Using this, the one-loop effective potential can be explicitly written as

TABLE VI. Two categories (tree-level and loop-level analysis) and four scenarios (according to whether $\lambda_2 > 0$ or $\lambda_2 < 0$) are summarized in the table.

Scenarios	Boundary lines	Symmetry breaking pattern
(tree) $\lambda_2 > 0$	Eq. (3.11)	$SU(N_c)\times U(N_s)\to SU(N_s)\times SU(N_c-N_s)\times U(1)$
(tree) $\lambda_2 < 0$	Eq. (3.12)	$SU(N_c)\times U(N_s)\to SU(N_c-1)\times U(N_s-1)\times U(1)$
(loop) $\lambda_2 > 0$	Eq. (G3)	$SU(N_c)\times U(N_s)\to SU(N_s)\times SU(N_c-N_s)\times U(1)$
(loop) $\lambda_2 < 0$	Eq. (G5)	$SU(N_c)\times U(N_s)\to SU(N_c-1)\times U(N_s-1)\times U(1)$

$$V = (a_1+\lambda_1)\left(\sum_{i=1}^{L}\rho_i^2\right)^2 + (a_2+\lambda_2)\sum_{i=1}^{L}\rho_i^4 + \frac{3g^4}{64\pi^2}\left(2\sum_{i=1}^{L}\sum_{j=1}^{i-1}(\rho_i^2+\rho_j^2)^2\log(\rho_i^2+\rho_j^2) + M_-^2\log(M_-) + M_+^2\log(M_+)\right), \quad (L=3) \quad \text{(H4)}$$

where $\rho_i^2+\rho_j^2 (i,j=1,2,3)$ are the six polynomial eigenvalues of the mass matrix M_{ab}^2 while M_+, M_- are the two nonpolynomial eigenvalues, written explicitly as

$$M_\pm = \frac{2}{3}\left(\rho_1^2+\rho_2^2+\rho_3^2 \pm \sqrt{\rho_1^4-\rho_2^2\rho_1^2-\rho_3^2\rho_1^2+\rho_2^4+\rho_3^4-\rho_2^2\rho_3^2}\right), \quad \text{(H5)}$$

and a_1, a_2 are the counter-terms which are determined through the Coleman-Weinberg renormazliation conditions.

The Coleman-Weinberg conditions are

$$\frac{1}{4N_c(N_c-1)}\sum_{i-1}^{N_c}\sum_{j=1}^{i-1}\frac{\partial^4 V}{\partial\rho_i^2\partial\rho_j^2}\bigg|_{\rho_i=\kappa_i M_R} = \lambda_1 \quad (N_c \geq N_s)$$
$$\frac{1}{4!N_c}\sum_{i=1}^{N_c}\frac{\partial^4 V}{\partial\rho_i^4}\bigg|_{\rho_i=\kappa_i M_R} = \lambda_1+\lambda_2, \quad \text{(H6)}$$

where M_R is the renormalization scale and κ_i represents the relative ratio between different scales. Using Eq. (H6), we can determine a_1, a_2. Inserting the result into Eq. (H4), we further obtain the full expression for the effective potential $V_{\text{eff}}^{1\text{loop}}$. This expression is extremely long and not particularly illuminating, so we do not present it.

The next step is to study the one-loop level VEV conditions that determine the boundary sheets (or lines) between the unbroken and broken phases. The vacuum configurations and symmetry-breaking patterns are determined from the κ_i and as discussed in Sec. III B, there is no alternative vacuum configuration found except for $\kappa_i = 1$ $(i=1,2,3)$ or $\kappa_i = \delta_{i1}$ $(i=1,2,3)$.

In the following, we illustrate the case $\kappa_i = 1$ $(i=1,2,3)$ as an example. The VEV condition is

$$\lim_{\kappa_3\to 1}\frac{\partial V_{\text{eff}}^{1\text{loop}}}{\partial\rho_i}\bigg|_{\substack{\rho_3=\kappa_3 M_R \\ \rho_1=\rho_2=M_R}} = 0 \quad (i=1,2,3), \quad \text{(H7)}$$

where the limit is implemented to get rid of the singularity, providing the following constraint

$$\frac{2}{81}M^3\left(-\frac{199g^4}{\pi^2}+486\lambda_1+162\lambda_2\right) = 0, \quad \text{(H8)}$$

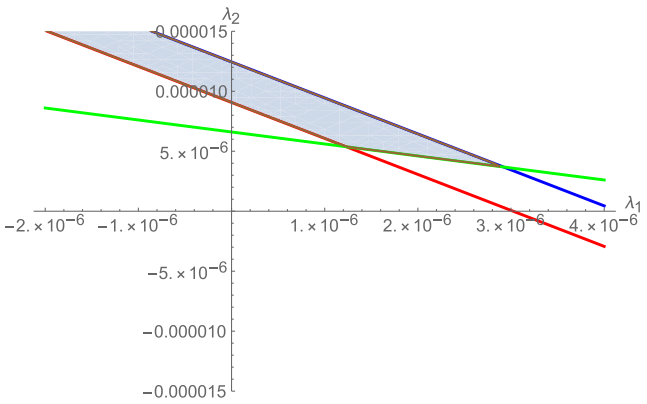

FIG. 16. In this figure, we choose a particular slice $g = 0.1$. The shaded region represents the broken phases $SU(N_c)\times U(N_s) \to SU(N_c-N_s)\times SU(N_s)\times U(1)$.

which corresponds to the blue line in Fig. 16. All three constraints are equivalent because of the permutation symmetry among ρ_1, ρ_2, ρ_3. The couplings satisfying the above constraint Eq. (H8) are evaluated at the broken scale in the Coleman-Weinberg scheme, whereas the couplings satisfying the constraint Eq. (G3) are evaluated at the broken scale in the Minimal-Subtraction scheme. We shall see that the coupling values evaluated in these two schemes are quite different.

In order to make sure the solutions are at a local minimum, the mass eigenvalues of the Hessian mass matrix

$$M_{ij} = \lim_{\kappa_3\to 1}\frac{\partial^2 V_{\text{eff}}^{1\text{loop}}}{\partial\rho_i\partial\rho_j}\bigg|_{\substack{\rho_3=\kappa_3 M_R \\ \rho_1=\rho_2=M_R}} \quad \text{(H9)}$$

must be non-negative. This yields

$$\frac{2}{27}\left(-\frac{145g^4}{\pi^2}+486\lambda_1+162\lambda_2\right) \geq 0,$$
$$-\frac{845g^4}{108\pi^2}+12\lambda_1+12\lambda_2 \geq 0, \quad \text{(H10)}$$

which correspond to the red and green lines in Fig. 16, respectively.

It is clear that when the RG flows run into the shaded region shown in Fig. 16, the symmetry is broken and we have the symmetry-breaking pattern $SU(N_c)\times U(N_s) \to SU(N_c-N_s)\times SU(N_s)\times U(1)$. Comparing Fig. 16 with Fig. 12, the shape and the structure of the shaded regions are very similar and consistent, while the coupling solutions are very different in the different schemes. In the Coleman-Weinberg scheme, both quartic couplings could be positive and at the same time symmetry breaking is driven by the loop contributions. In the minimal subtraction scheme, one of the two quartic couplings is always negative.

[1] D. J. Gross and F. Wilczek, Phys. Rev. D **8**, 3633 (1973).
[2] D. J. Gross and F. Wilczek, Phys. Rev. Lett. **30**, 1343 (1973).
[3] D. J. Gross and F. Wilczek, Phys. Rev. D **9**, 980 (1974).
[4] H. D. Politzer, Phys. Rev. Lett. **30**, 1346 (1973).
[5] C. Pica and F. Sannino, Phys. Rev. D **83**, 035013 (2011).
[6] D. F. Litim and F. Sannino, J. High Energy Phys. 12 (2014) 178.
[7] T. P. Cheng, E. Eichten, and L. F. Li, Phys. Rev. D **9**, 2259 (1974).
[8] D. J. E. Callaway, Phys. Rep. **167**, 241 (1988).
[9] G. F. Giudice, G. Isidori, A. Salvio, and A. Strumia, J. High Energy Phys. 02 (2015) 137.
[10] B. Holdom, J. Ren, and C. Zhang, J. High Energy Phys. 03 (2015) 028.
[11] C. Pica, T. A. Ryttov, and F. Sannino, Phys. Rev. D **96**, 074015 (2017).
[12] E. Molgaard and F. Sannino, Phys. Rev. D **96**, 056004 (2017).
[13] H. Gies and L. Zambelli, Phys. Rev. D **96**, 025003 (2017).
[14] M. B. Einhorn and D. R. T. Jones, Phys. Rev. D **96**, 055035 (2017).
[15] D. F. Litim, M. Mojaza, and F. Sannino, J. High Energy Phys. 01 (2016) 081.
[16] J. K. Esbensen, T. A. Ryttov, and F. Sannino, Phys. Rev. D **93**, 045009 (2016).
[17] G. M. Pelaggi, F. Sannino, A. Strumia, and E. Vigiani, Front. Phys. **5**, 49 (2017).
[18] K. Intriligator and F. Sannino, J. High Energy Phys. 11 (2015) 023.
[19] B. Bajc and F. Sannino, J. High Energy Phys. 12 (2016) 141.
[20] S. Abel and F. Sannino, Phys. Rev. D **96**, 056028 (2017).
[21] L. E. Ibanez and G. G. Ross, Phys. Lett. **110B**, 215 (1982).
[22] A. Eichhorn and A. Held, arXiv:1705.02342.
[23] N. Christiansen, A. Eichhorn, and A. Held, Phys. Rev. D **96**, 084021 (2017).
[24] N. Christiansen and A. Eichhorn, Phys. Lett. B **770**, 154 (2017).
[25] K. A. Intriligator and N. Seiberg, Nucl. Phys. B, Proc. Suppl. **45**, 1 (1996); Subnuclear series **34**, 237 (1997).
[26] A. Kagan, *Proceedings of the Particle Physics from Underground to Heaven, Baltimore, 1991*, pp. 217–242; New York City University Report No. CCNY-HEP-91-12.
[27] B. A. Dobrescu, Nucl. Phys. **B449**, 462 (1995).
[28] A. L. Kagan, Phys. Rev. D **51**, 6196 (1995).
[29] W. Altmannshofer, S. Gori, A. L. Kagan, L. Silvestrini, and J. Zupan, Phys. Rev. D **93**, 031301 (2016).
[30] D. B. Kaplan and H. Georgi, Phys. Lett. **136B**, 183 (1984).
[31] D. B. Kaplan, H. Georgi, and S. Dimopoulos, Phys. Lett. **136B**, 187 (1984).
[32] M. J. Dugan, H. Georgi, and D. B. Kaplan, Nucl. Phys. **B254**, 299 (1985).
[33] F. Sannino, A. Strumia, A. Tesi, and E. Vigiani, J. High Energy Phys. 11 (2016) 029.
[34] G. Cacciapaglia, H. Gertov, F. Sannino, and A. E. Thomsen, arXiv:1704.07845.
[35] D. B. Kaplan, Nucl. Phys. **B365**, 259 (1991).
[36] F. Sannino, Acta Phys. Pol. B **40**, 3533 (2009).
[37] G. Cacciapaglia and F. Sannino, J. High Energy Phys. 04 (2014) 111.
[38] S. R. Coleman and E. J. Weinberg, Phys. Rev. D **7**, 1888 (1973).
[39] E. Gildener and S. Weinberg, Phys. Rev. D **13**, 3333 (1976).
[40] E. Gildener, Phys. Rev. D **13**, 1025 (1976).
[41] M. E. Machacek and M. T. Vaughn, Nucl. Phys. **B249**, 70 (1985).
[42] O. Antipin, M. Gillioz, E. Molgaard, and F. Sannino, Phys. Rev. D **87**, 125017 (2013).
[43] I. Jack and H. Osborn, Nucl. Phys. **B343**, 647 (1990).
[44] H. Osborn, Phys. Lett. B **222**, 97 (1989).
[45] W. E. Caswell, Phys. Rev. Lett. **33**, 244 (1974).
[46] T. Banks and A. Zaks, Nucl. Phys. **B196**, 189 (1982).
[47] L. F. Li, Phys. Rev. D **9**, 1723 (1974).
[48] S. Weinberg, Phys. Lett. **82B**, 387 (1979).
[49] W. A. Bardeen, Report No. FERMILAB-CONF-95-391-T, 1995.
[50] C. T. Hill, Phys. Rev. D **89**, 073003 (2014).
[51] Z. W. Wang, T. G. Steele, T. Hanif, and R. B. Mann, J. High Energy Phys. 08 (2016) 065.
[52] T. G. Steele, Z. W. Wang, D. Contreras, and R. B. Mann, Phys. Rev. Lett. **112**, 171602 (2014).
[53] T. G. Steele and Z.-W. Wang, Phys. Rev. Lett. **110**, 151601 (2013).
[54] T. G. Steele, Z. W. Wang, and D. G. C. McKeon, Phys. Rev. D **90**, 105012 (2014).
[55] J. A. Casas, J. R. Espinosa, M. Quiros, and A. Riotto, Nucl. Phys. **B436**, 3 (1995); **B439**, 466(E) (1995).
[56] E. S. Fradkin and A. A. Tseytlin, Nucl. Phys. **B201**, 469 (1982).
[57] I. L. Buchbinder, S. D. Odintsov, and I. L. Shapiro, *Effective Action in Quantum Gravity* (IOP, Bristol, 1992).
[58] W. Gellert, H. Küstner, M. Hellwich, and H. Kästner, *The Concise Encyclopedia of Mathematics* (Springer, New York, 1975).
[59] R. Jackiw, Phys. Rev. D **9**, 1686 (1974).